Ar-Ar ages and ore-forming material sources of the Na Bop-Pu Sap Pb-Zn Deposit in the Cho Don Area, Northeastern Vietnam

Khuong The Hung [1]*✉ ⓘ, Pham Trung Hieu [2]✉ ⓘ, Ngo Xuan Dac [3]✉, Nguyen Duy Hung [1]✉

[1] *Hanoi University of Mining and Geology, Hanoi, Vietnam*
[2] *University of Science, Ho Chi Minh, Vietnam*
[3] *Vietnam Institute of Geosciences and Mineral Resources, Hanoi, Vietnam*
Corresponding author: e-mail khuongthehung@humg.edu.vn

Abstract

Purpose. This study aims to investigate the ore mineralization characteristics and genesis models and assess the mineral potential of the Na Bop-Pu Sap lead-zinc deposit, which represents a novel deposit type in northeastern Vietnam.

Methods. This research employs several analytical methods, including microscopic analysis of ore minerals, sulfur and lead isotope analysis of ore sulfide minerals, Ar-Ar dating of sericite samples contemporaneous with sulfide ores, and fluid inclusion studies to determine ore-forming temperatures.

Findings. Field observations suggest that the ore deposits manifest as Pb-Zn-bearing veins along faults and as strata-bound ore types within early Devonian sedimentary carbonate rocks. Microscopic analysis identifies galena, sphalerite, pyrrhotite, pyrite, and arsenopyrite as ore minerals, accompanied by gangue minerals such as quartz, calcite, and dolomite. Sulfur-isotope values ($\delta^{34}S$) of galena, sphalerite, and pyrite range from +0.10 to +8.49‰ (mean = +4.48‰), suggesting a magmatic origin with a deep source. Lead isotope ratios of galena ($^{206}Pb/^{204}Pb$: 18.451-18.651, $^{207}Pb/^{204}Pb$: 15.685-15.836, $^{208}Pb/^{204}Pb$: 38.909-39.501) point to an upper crustal source. Ar-Ar dating of sericite yields plateau ages of 237.1 ± 2.3 Ma and 242.6 ± 2.4 Ma, correlating with the timing of lead-zinc mineralization, as indicated by the syntectonic texture between sericite minerals and sulfide ores. Fluid inclusion studies on calcite from galena-hosted veins suggest moderate temperatures (201-245°C) and salinities (4.65-8.00 wt.% NaCl equiv.), indicative of evolving $H_2O - NaCl$ systems and variable physico-chemical conditions. These findings classify the Na Bop-Pu Sap deposit as an epithermal-type deposit.

Originality. The Na Bop-Pu Sap Pb-Zn deposit in northern Bac Kan Province, Vietnam, is one of the largest deposits in the Cho Don area. It is notable for its significant reserves and unique metal combination. Despite extensive knowledge of Pb-Zn mineralization, the timing and origin of ore-forming fluids remain poorly understood.

Practical implications. This study provides insights into the genesis and spatio-temporal evolution of Pb-Zn mineralization in the Na Bop-Pu Sap deposit within the Cho Don area.

Keywords: Na Bop-Pu Sap deposit, Cho Don area, Pb-Zn mineralization, lead, sulfur, Ar-Ar isotope data

1. Introduction

Carbonate-hosted lead-zinc deposits exhibit diverse characteristics, as documented by Sangster (1996) [1]. Vietnam is host to over 74 known lead-zinc deposits, as reported by Tri et al. (2011) [2]. Notably, the Cho Don-Cho Dien lead-zinc ore (CDO-CDI) districts have been identified among these deposits. Although certain deposits were investigated and exploited over the past few decades, the ore reserves could be more considerable, with the majority falling within the small to medium scale. The distribution of lead-zinc ores spans provinces such as Bac Kan, Tuyen Quang, Cao Bang, Ha Giang, Thai Nguyen, Lang Son, Lao Cai, Yen Bai, Lai Chau, Dien Bien, Hoa Binh, etc. These deposits can be classified into two primary groups: the initial group encompasses those in carbonate and terrigenous-carbonate formations, whereas the second group consists of deposits in intrusive and effusive rocks [2]. Regarding mineral composition, certain deposits and ore incidents manifest both sulphide and oxidation types.

The concentration of lead-zinc mineralization is most pronounced in the Paleozoic geological structures of the Northeast region of Vietnam, particularly within the Lo Gam structural zone or along the boundary between the Lo Gam and the Phu Ngu structural zones. Tectonically, these structures are part of the fold-and-thrust belt of the North Vietnam-South China Block [3]-[7]. The geological formations containing lead-zinc mineralization within these structures consist of carbonate and terrigenous-carbonate sedimentary sequences of the early to middle Paleozoic age. These sequences host numerous lead-zinc mineral occurrences, either in ore deposits or mineralized occurrences, primarily concentrated in two central ore districts known as the CDI and CDO districts. Deposits such as Na Bop-Pu Sap, Lung Vang, Ba Bo, and Na Tum are within the CDO district.

The genesis model and timing of lead-zinc mineralization in the Cho Don region remain debatable, mainly because no study has yet provided reliable direct age determinations for the mineralization or a clear understanding of the source of ore-forming materials. Previous perspectives suggested that the lead-zinc deposits in the Cho Don area were linked to the granite rocks of the Phia Bioc complex based on lead model ages and elevated Pb and Zn concentrations in these granites [8], [9]. Upon examining the ore characteristics, lead-zinc deposits in the CDO-CDI districts have been classified as MVTy deposits [10], SEDEX deposits [4], [5], [11], or as sediment-hosted deposits [12]. Nevertheless, recent studies propose that the lead-zinc ore at the Na Bop-Pu Sap deposit (NPD) may be linked to the origin of granites at a more profound, more ancient age than the Phia Bioc complex [13], [14]. Therefore, conducting detailed and comprehensive research on the characteristics of lead-zinc mineralization in the area is crucial for elucidating the origin and mineral prospects, which are essential.

This study focuses on the NPD as a key area for investigating ore mineralization characteristics and genesis models and assessing mineral potential, representing a novel deposit type in northeastern Vietnam. The research provides a detailed analysis of the structural, textural, and mineralogical features of the ore-bearing horizons, the geochronology of the host rocks associated with lead-zinc mineralization, and the sulfur and lead isotopic signatures that contributed to the deposit's formation.

2. Geological setting

2.1. Regional geology

The Lo Gam folded structure, which covers most of the Song Lo zone area [15], except the Song Chay granite massif, was later termed the Song Gam anticlinorium by Tri et al. (1977) [16]. More recently, it has been referred to as the western Viet Bac zone [2]. Located in northeastern Vietnam, the Lo Gam structural zone lies adjacent to the southwest's Song Hong strike-slip fault zone (Fig. 1).

Its boundaries include the Song Chay dome to the northwest, representing an exposure of the Precambrian basement of the Yangtze Platform, and the Mesozoic Song Hien and An Chau basins to the northeast and southeast, respectively. The dominant geological features of the region include sedimentary-metamorphic units from the Early and Middle Paleozoic, primarily consisting of carbonate rocks interbedded with sandstone, schist, conglomerate, and gravelstone. Felsic volcanic rocks, particularly in the Na Son ore district to the north, play a significant role alongside widespread igneous rocks across the Lo Gam structure. The Phia Bioc complex, composed of high-alumina biotitic granites, is prevalent, forming plutons that conform to the arched fault systems surrounding and penetrating the Paleozoic sediments. These granitoids are spatially linked to Pb-Zn deposits, particularly in the CDO and CDI districts. Additionally, areas with small plutons and dikes of alkali syenites, gabbro-peridotites from the Nui Chua complex, and gabbro-dolerites from the Cao Bang complex are present. In the southern region, the Nui Dieng complex comprises calc-alkaline granites, granodiorites, and diorites, forming small northwest-trending plutons in the Thai Nguyen ore district, often associated with Sn deposits. The majority of the region's igneous rocks were emplaced during the Permo-Triassic period

(233-251 Ma), influenced either by the Emeishan plume or by the collision between the Sibumasu and Indochina blocks, as indicated by recent dating of rocks within the Lo Gam structure and neighboring areas [17]-[21].
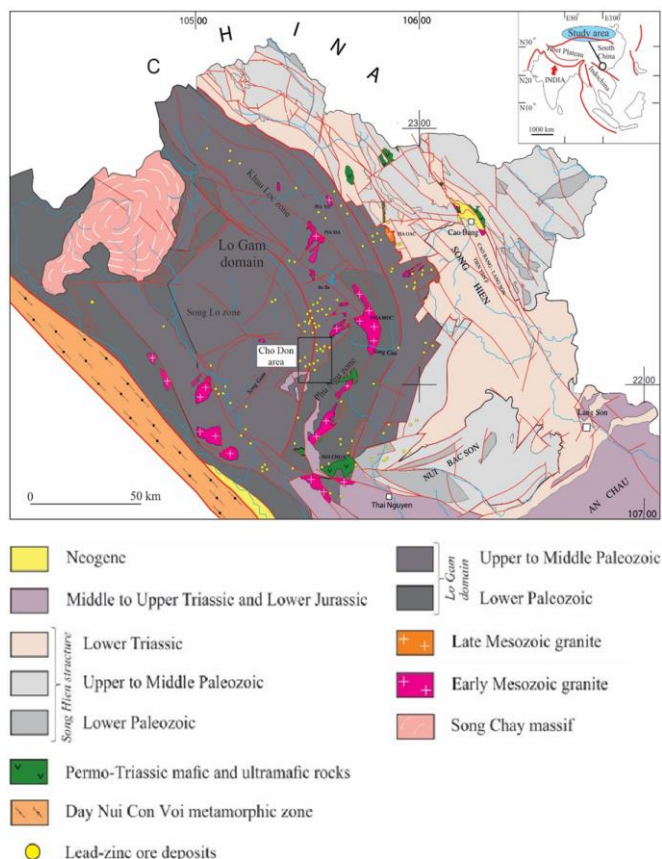

Figure 1. Regional structural map of Northeastern Vietnam showing the lead-zinc deposits and occurrences (modified from [22], [23])

The CDO district (Bac Kan) is situated east of the Lo Gam structure, about 75 km north of Thai Nguyen city (Fig. 1). The primary Pb-Zn mineralized veins are mainly located within early Devonian carbonate rocks of the Co Xo and Phia Phuong formations. A smaller number of mineral veins are found within the late Ordovician to early Silurian sediments of the Phu Ngu formation. These formations consist of quartz-sericite schist, clay schist, limestone schist with limestone, siliceous limestone, and clay schist interlayered with quartzite, albite tuff, and sandstone tuff. The rocks show deformation through short folds and are crosscut by various fracture systems. Pb-Zn mineralization is predominantly concentrated in the Devonian carbonate sediments, especially at the intersections of northeast-southwest and northwest-southeast trending structures (Fig. 2) [24].

The mineralized zone is associated with gray limestones interlayered with calcite, sericite schist, and sandstone tuff. Mineralized clusters such as Ba Bo, Lung Vang, Na Bop, Na Tum, and Pu Sap have been identified within the CDO district. The ore in these clusters exhibits a disseminated-vein structure, with rare occurrences of massive structures [2]. The mineral composition across all mineralized clusters is relatively consistent, with sphalerite and galena being the dominant ore minerals, with galena being more prevalent. Other minerals present include pyrrhotite, pyrite, arsenopyrite, and chalcopyrite.
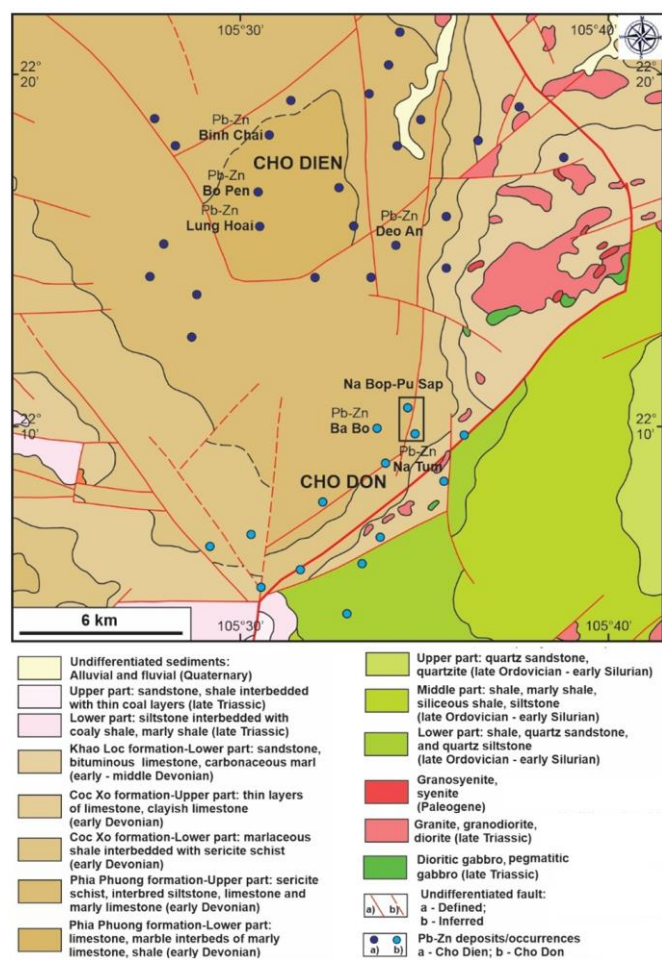
Figure 2. Geological map of the CDO-CDI area showing locations of the Pb-Zn deposits and occurrences (modified from [14], [25], [26])

Less common minerals include tetrahedrite, stannite, cassiterite, native bismuth, and monazite [24].

2.2. Major structures and tectonics

The CDO-CDI area exhibits a standard geological structure identified as a large anticlinorium zone, known as the Phia Khao anticlinorium zone [15], also referred to as the North Vietnam folded zone, formed during the Late Caledonian orogeny [16]. Contributing to the structural complexity of the Cho Don area are several petrotectonic associations, including The petrotectonic associations of the lower to middle Paleozoic continental margin (Late Ordovician – Early Silurian), exhibiting folding related to early Paleozoic orogeny, particularly in the southeast. This includes the original formations of the Phu Ngu formation. The petrotectonic associations of the Devonian orogenic phase occupy a significant portion of the study area. It consists of original carbonate formations, carbonate-siliciclastic rocks, and felsic-alkaline volcanic rocks containing Mn-Fe mineralization. The rocks undergo intense thermal metamorphism and exhibit strong karstification, characterized by closely spaced folds (Phia Khao). Last, the petrotectonic associations of the Upper Triassic orogenic phase are confined to the eastern Ngoc Hoi area, consisting of limestones with thin coal beds belonging to the Van Lang formation.

Tectonic activity has been notably robust in the CDO-CDI area, evidenced by intense folding and the development of complex fault systems (Fig. 2). Noteworthy fault systems include A circular fault system, with significant roles played by the faults along National Highway 3A (Cho Moi – Cao Ky – Pac Nam fault), dividing the Lo Gam, Song Hien zones and the fault system of Song Day – Cho Don – Ba Be – Ban Mu, intersecting the Phu Ngu anticlinorium zone. These faults, with lengths ranging from 50-100 km, have broad shear zones and dip toward the NWW with angles of 80-85°.

The NW-SE-trending fault system comprises faults along the Song Lo, upper reaches of the Song Gam, Song Quang rivers, and the Nguyen Binh area. These faults, likely active since the early Paleozoic, have experienced multiple reactivations [25]. This fault group is often displaced by east-west or northeast-southwest-trending faults with displacements ranging from 0.5-1.0 km. Most of these faults have lengths exceeding 50 km, dipping toward the southwest with slopes of 70-80°. Along these faults are shear zones 5-7 km wide, invaded by granitoids and mafic rocks. Another one is the northeast-southwest-trending fault system, and a transverse northeast-southwest fault system is developed in the Na Mong, Ninh Kiem - Pac Van, Cho Don, Phia Khao, and Pia Ma areas. These faults, with lengths ranging from 5-30 km, have slopes of 80-85° and displacements of 0.3-1.0 km. The northeast-southwest-trending fault system often consists of younger faults cutting through various geological structures and other fault groups, having steep dips, 2-15 km lengths, and scattered distribution in the Dai Thi area.

3. Geology of the NPD

The NPD is located in the CDO area at an altitude ranging from approximately 300 to 600 m above sea level. Extensive exploration boreholes were drilled at NPD, identifying three ore bodies and eight mineralized bodies [24], [27]. While orebodies TQ.1 and TQ.2 are partially exposed on the surface, orebody TQ.4 remains concealed (Figs. 3, 4).

The open-pit mining operation at the NPD has been terminated and repurposed as a waste dump. The Bac Kan Minerals Joint Stock Company (BAMCORP) is currently employing subterranean mining methods for ore extraction, utilizing shafts and longwalls at levels +230, +210 m (Pu Sap area), and +360, +320 m (Na Bop area). Our ongoing research relies on samples collected from drill cores and longwalls within the NPD.

3.1. Stratigraphy and lithology

The predominant strata exposed in the NPD area are from the Devonian period (Fig. 3). The Lower Devonian formation consists of carbonate and terrigenous-carbonate sequences, specifically the Coc Xo formation. The lithostratigraphic units of the Coc Xo formation predominantly trend in a south-to-north direction, with dipping angles ranging between 25 and 45° towards the east and southeast. In regions near fault zones, the rock formations are overturned and display directional instability, with steeper dip angles between 50 and 70°. In the western part of the Na Bop area, the formation is divided into two subformations. The Lower Subformation is restricted to a narrow zone west of Na Bop and is primarily composed of phyllite, quartzite, and quartz-sericite. It trends approximately north-south and dips eastward. This subformation shows limited occurrences of lead and zinc ore bodies and has a thickness exceeding 1300 m. The Upper Subformation, which dominates much of the study area, is frequently subdivided into distinct blocks by fault systems.
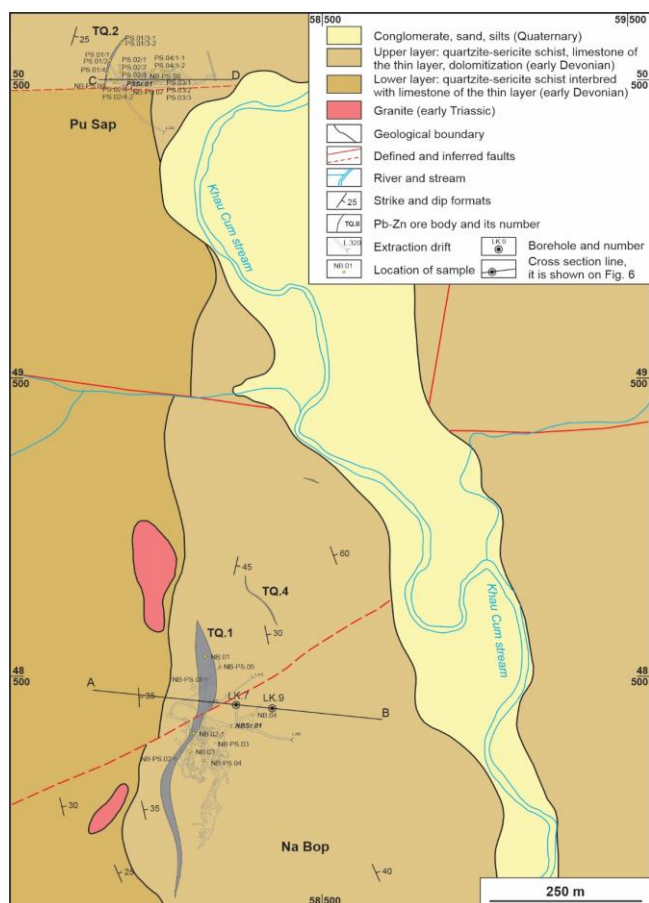
Figure 3. Simplified geological map of the NPD (modified from [14], [27])
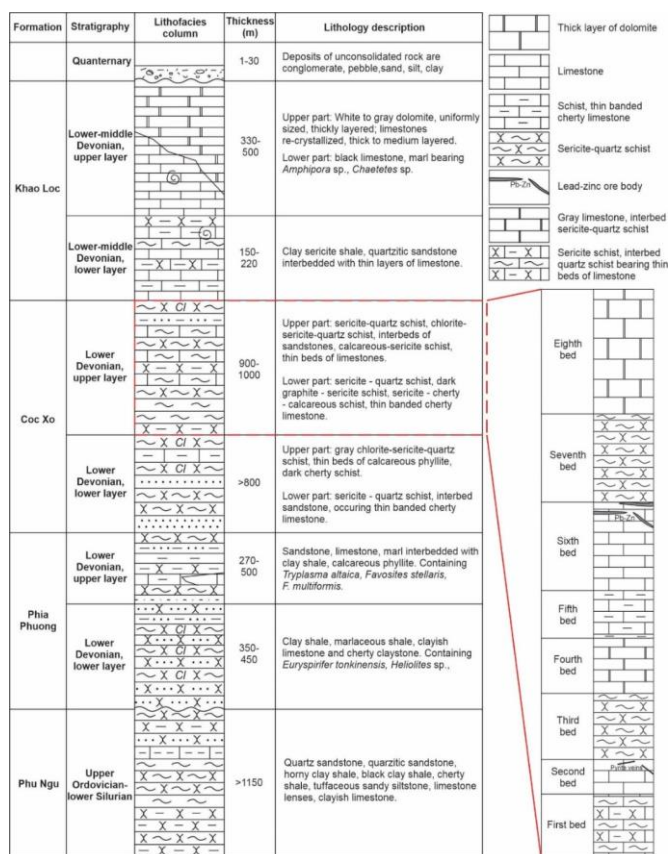

Figure 4. Schematic stratigraphic column of the CDO area, showing the detailed lithologic units of the Coc Xo Formation in the NPD (the stratigraphic column is after [25])

The rocks within this subformation undergo significant alteration due to metamorphic processes, including exchange reactions and thermal metamorphism. The Upper Subformation can be divided into eight distinct beds, arranged from bottom to top (Fig. 4) [25], as follows: The first bed is mainly composed of sericite phyllite, interspersed with thin layers of limestone, and occasionally exhibits color variations of chalky lime and light gray. The thickness of this bed ranges from 50 to 85 m. Above the first, the second bed consists of limestone intercalated with thin layers of sericite phyllite. Rich pyrite ore veins have been identified within this bed, which is 35 to 50 m thick. The third bed is predominantly sericite phyllite, occasionally interspersed with thin layers of gray or light gray chalky lime lenses. The rock is compressed and thinly layered, with a thickness ranging from 45 to 90 m. The fourth bed comprises gray limestone intercalated with sericite phyllite, often altered and mildly dolomitized, with a faint pink hue. The thickness of this bed varies between 25 and 75 m. The fifth bed consists of multiple layers of phyllite intercalated with thin limestone layers, with a thickness ranging from 50 to 65 m. The sixth bed, primarily limestone, is the main ore-bearing layer for Pb and Zn. This bed exhibits directional instability and severe fracturing due to fault systems, with a 50 to 120 m thickness. The seventh bed, located above the ore, is composed of sericite phyllite, especially in the TQ.1 ore body area.

The rock formations in this layer are intensely folded and altered. Pb and Zn ore bodies are predominantly found within the limestone or in the transition zone between limestone and phyllite, where oxidation is less pronounced, often forming thick ore bodies ranging from 90 to 120 m in thickness.

The eighth bed is a layer of brightly colored, altered limestone, occurring as blocks or thickly layered, mainly in the northeast corner of the Na Bop area. The thickness of this bed ranges from 90 to 200 m. Therefore, the total thickness of the Upper Subformation exceeds 800 m.

3.2. Igneous rocks

Intrusive magmatic rocks, including the biotite granite porphyry of the Phia Bioc complex, are characteristic features of the study area. These rocks are exposed as small blocks, such as the Cho Don granite massif, in the southern and northeastern parts of the CDO-CDI area (Fig. 2) [25]. Notably, the Cho Don granite massif is near the TQ.1 lead-zinc body (Fig. 3).

The Phia Bioc granite-biotite complex was first described by Izokh [15]. In the studied region, the Phia Bioc complex is bounded by faults to the southeast (Fig. 2). To the east, granite massifs belonging to the Phia Bioc complex intrude into the limestones and shales of the Coc Xo Formation, causing hornfelsification within a zone approximately 200 m wide. The age of the high-alumina granites in the Phia Bioc complex has been determined using U-Pb dating of cordierite granite from the Kim Boi massif [5], yielding a concordant isotopic age of 242.4 ± 2.2 Ma, placing it in the Middle Triassic. Additionally, the $^{39}Ar/^{40}Ar$ dating of Cho Don granite provided an age of 250.5 ± 1.0 Ma [5], suggesting that the high-alumina granites of the Phia Bioc complex formed around the Early-Middle Triassic boundary. As a result, many geologists have interpreted the Phia Bioc complex as a product of the collision between the Sibumasu and Indochina blocks during the closure of the Paleo-Tethys Ocean from the

83

Late Permian to the Middle Triassic [22], [28]-[31]. Alternatively, some researchers associate it with the Emeishan Large Igneous Province [5], [20], [32].

3.3. Tectonics

The NPD is located on the southeastern limb of the Phia Khao anticlinorium and is characterized by two distinct fault systems: the NW-SE and NE-SW fault systems. The lead-zinc mineralization is primarily concentrated along the NW-SE fault system, where one of the faults acts as a conduit for ore-forming fluid migration (Fig. 5a-d).

Conversely, the NE-SW fault system intersects the TQ.1 ore body, introducing complexities to the structural features of the mining site. This situation poses challenges for the exploration and exploitation of lead-zinc ore in the area, as outlined in the study by Bac (2011) [26].

The hanging wall rocks of the lead-zinc ore body exhibit brecciated limestones (Fig. 5d-e). The nature of the syntectonic texture of the sulfide ore and sericite minerals at NPD suggests a cogenesis between the sulfide ore and sericite minerals (Fig. 5h).
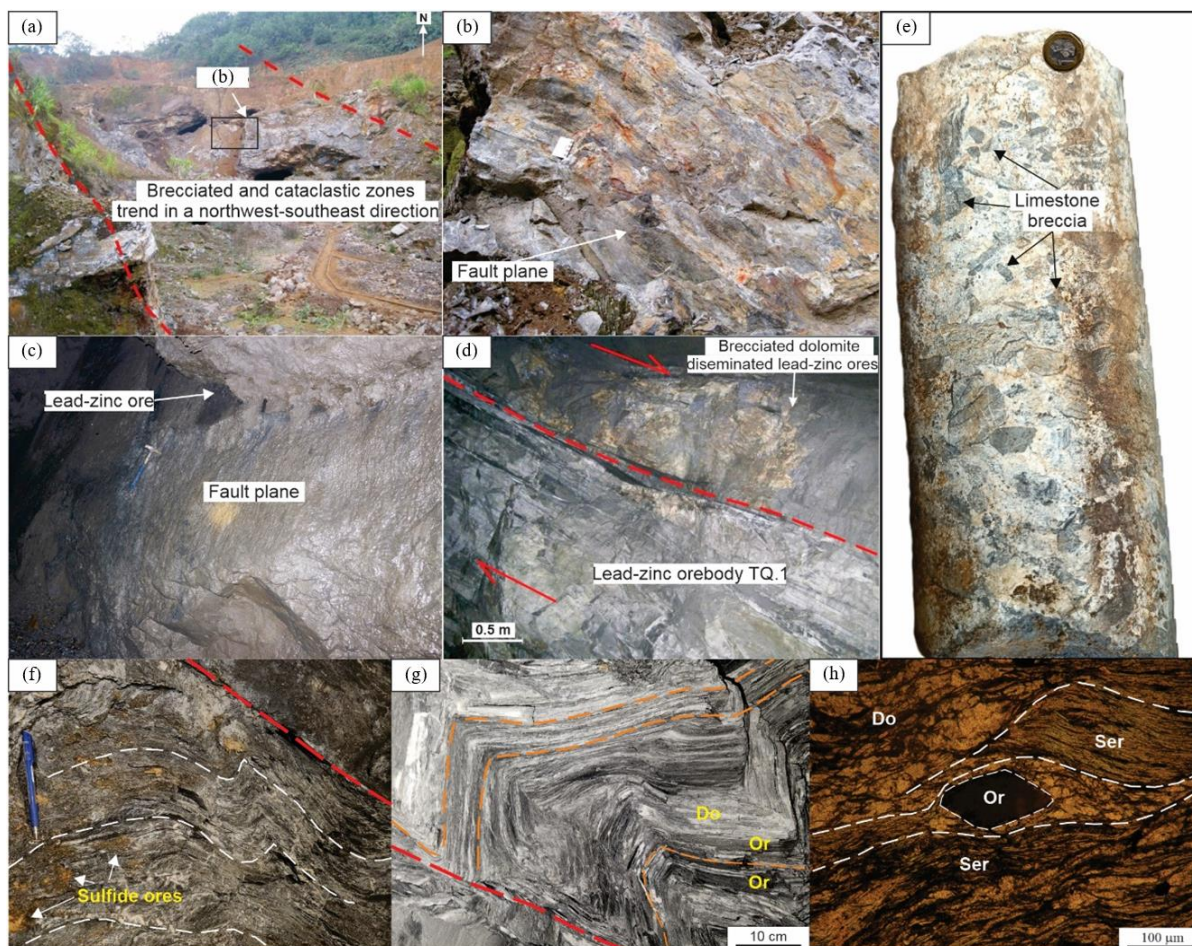

Figure 5. *The NW-SE-trending fault controls the distribution of lead-zinc ore at the NPD: (a)-(c) a brecciated zone and fault planes along this fault system, which governs the lead-zinc ore, observed both on the mining surface and along the longwall at a depth of 320 m; (d) brecciated dolomite is visible in the hanging wall of ore body TQ.1.; (e) a drill core sample of brecciated dolomite encountered at a depth of 40m under surface in the Pu Sap area (Fig. 5a, b, d from [14]); (f), (g) sulfide ore within the folded zone; (h) a syntectonic texture of the sulfide ore and sericite minerals is observed under the microscope*

3.4. Ore bodies

Three lead-zinc (Pb-Zn) ore bodies have been discovered in the mining vicinity, featuring two strata-bound ore types and one classified as an ore vein type. This vein-type ore body intersects the dolomite rocks within the Lower Devonian Coc Xo formation (Figs. 5, 6). The predominant ore bodies denoted as TQ.1, TQ.2, and TQ.4 orebodies, are sequentially positioned within the study area from the south to the north. The adjacent rocks consist primarily of modified limestone and dolomite. Alterations linked to the distinctive ore body involve dolomitization, chlorination, and intense dolomitization (Fig. 7a, d).

The TQ.1 ore body, located in the Na Bop area, extends approximately 700 m. It exhibits an elongated north-south

orientation and inclines towards the east at angles ranging from 25 to 55°, aligning with the bedding of the surrounding rock (Fig. 3, Fig. 6a). The boundary between the TQ.1 ore body and the adjacent rocks is clearly defined, with the ore body's thickness varying significantly from 10.34 to 3.85 m. The primary ore body is intersected by a NE-SW fault zone (Fig. 5a-c, 6a), indicating that this fault system occurred after ore mineralization, leading to the displacement of ore zones in the region.

Limestone chips are observed at the slip surface, suggesting deformation and a notable slip surface in the mining area. Calcite crystals were observed growing on the slip surfaces, although no apparent evidence of mineralization was associated with them (Fig. 5c, d).
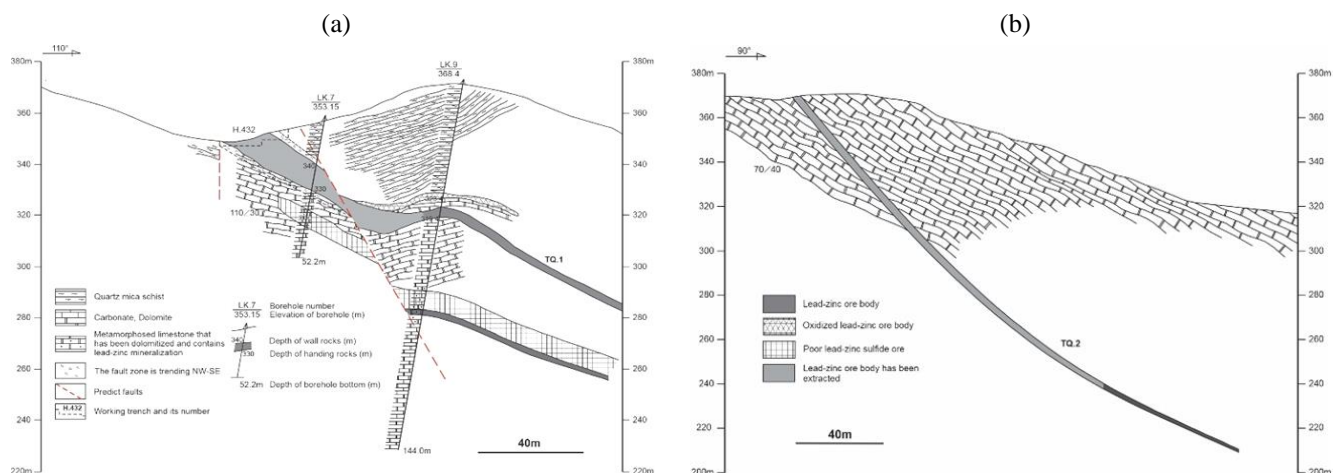
Figure 6. *Geological cross-sections of the NPD: (a) AB cross-section showing the TQ.1 ore body; (b) CD cross-section showing the TQ.2 ore body (modified from [24])*
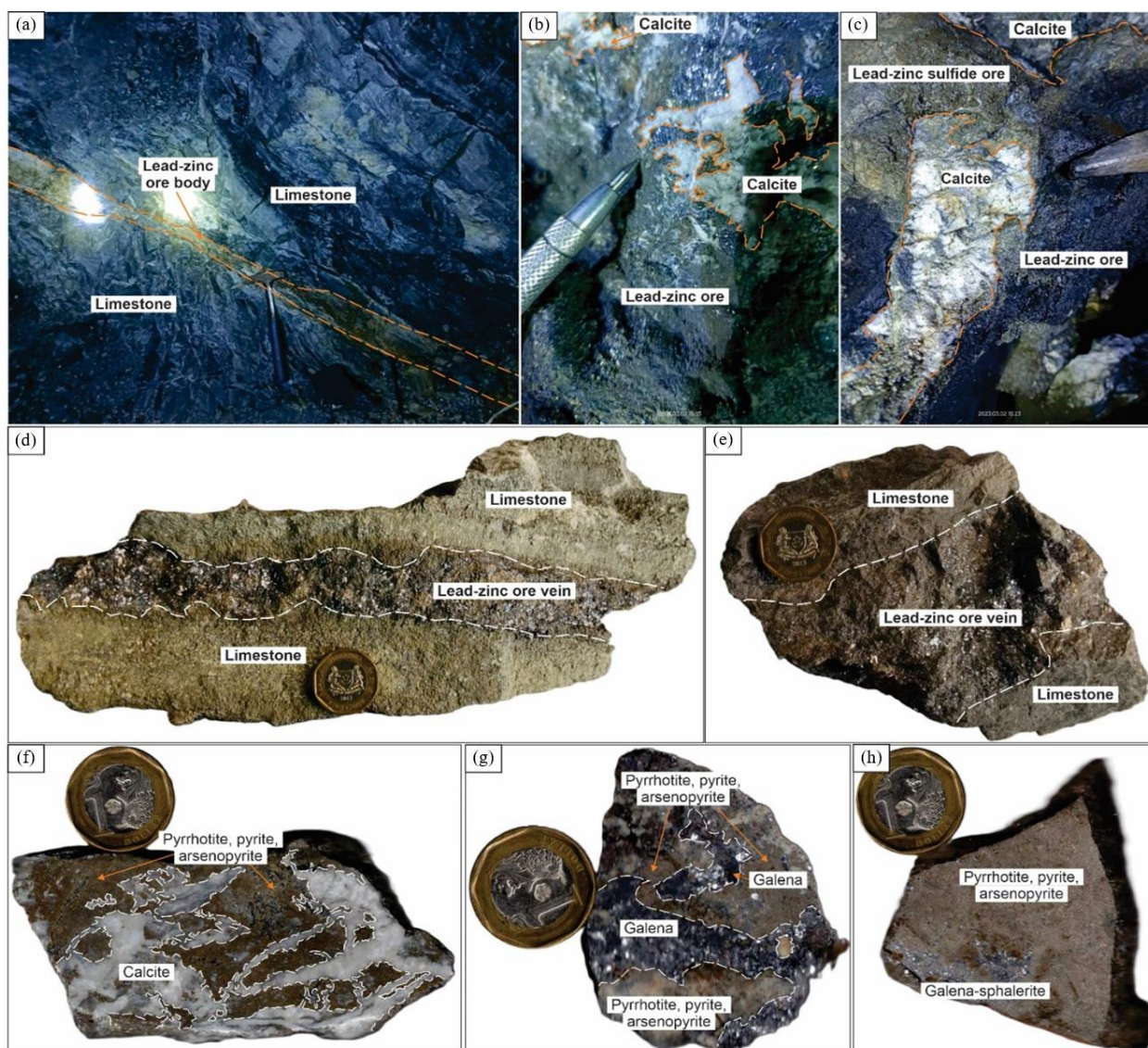
Figure 7. *Lead-zinc sulfide ores at the NPD: (a) ore body TQ.1 is conformable with surrounding limestone observed beneath the longwall at the +210 m level in the Na Bop area; (b), (c) disseminated Pb-Zn ore, filling the gaps and fractures of the calcite vein at the +320 m level of Na Bop area; (d), (e) vein-type Pb-Zn ore; (f), (g) disseminated sulfide Pb-Zn ore, filling gaps and cavities in the calcite vein; (h) Massive Pb-Zn ores*

The TQ.2 ore body, located in the Pu Sap area, lies approximately 1000 m from the TQ.1 ore body in the Na Bop area (Fig. 3). It extends in a NE-SW direction over a distance of 100-120 m, with dips of 35 to 40° towards the east-northeast. The ore body has been thoroughly mined through shafts down to a depth of +219.04 m (Fig. 6b). According to

mining records, the thickness of the ore body at depth is around 2.5 m and remains relatively consistent along the dip direction. Survey results show that the ore deposit primarily occurs in veins, filling fractures, and karst cavities developed along the NW-SE fault zone (Fig. 7b-f). On the mining surface, lead-zinc ore is extracted from karst cavities (Figs. 5a, 7g, h). Alterations related to the ore body include dolomitization and chlorination. The principal ore minerals are galena, sphalerite, pyrrhotite, and pyrite, with minor arsenopyrite and chalcopyrite. The ore structure consists of disseminations, veins, and ore bodies, exhibiting textures indicative of replacement and erosion. The lead and zinc ores concentrations generally decrease from the upper to the lower layers.

The TQ.4 ore body is located in the central part of the study area, roughly 100 meters north of TQ.1. It extends for about 50-60 meters in a NE-SW direction (Fig. 3). This ore body dips steeply. It intersects with altered limestone, filling fractures. The primary ore minerals are sulfides, including pyrite, sphalerite, and galena. Additionally, smaller lead-zinc ore bodies are found within quartz-mica schists and carbonate rocks; however, these have garnered limited attention due to their questionable economic potential.

3.5. Ore textures and structures

3.5.1. Types of ores and their properties

In nature, common primary ore minerals comprise galena, pyrite, pyrrhotite, and sphalerite (> 5%), followed by arsenopyrite (1-5%) and, less commonly (< 1%), chalcopyrite. Galena is frequently observed in the samples with an uneven distribution; some samples contain only a few small grains, while others exhibit concentrations ranging from 1-5%. Galena can be categorized into two generations: Galena I manifests as anhedral grains, with a minimal presence of semi-euhedral grains varying in size from 0.01-1 mm. Galena I aggregates into small clusters, irregularly dispersed on the rock matrix (Fig. 8n), or fills the fracture veins of fractured rocks, forming continuous or discontinuous veinlets. Galena I, sphalerite I, chalcopyrite I, and pyrite I create a symbiotic mineral assemblage distributed as nests, clusters, or vein networks within the rock matrix (Fig. 8n, o). Galena II appears as anhedral grains associated with sphalerite II, quartz, and calcite during the late stage of ore formation, forming cross-cutting veinlets across pre-existing minerals and ores.
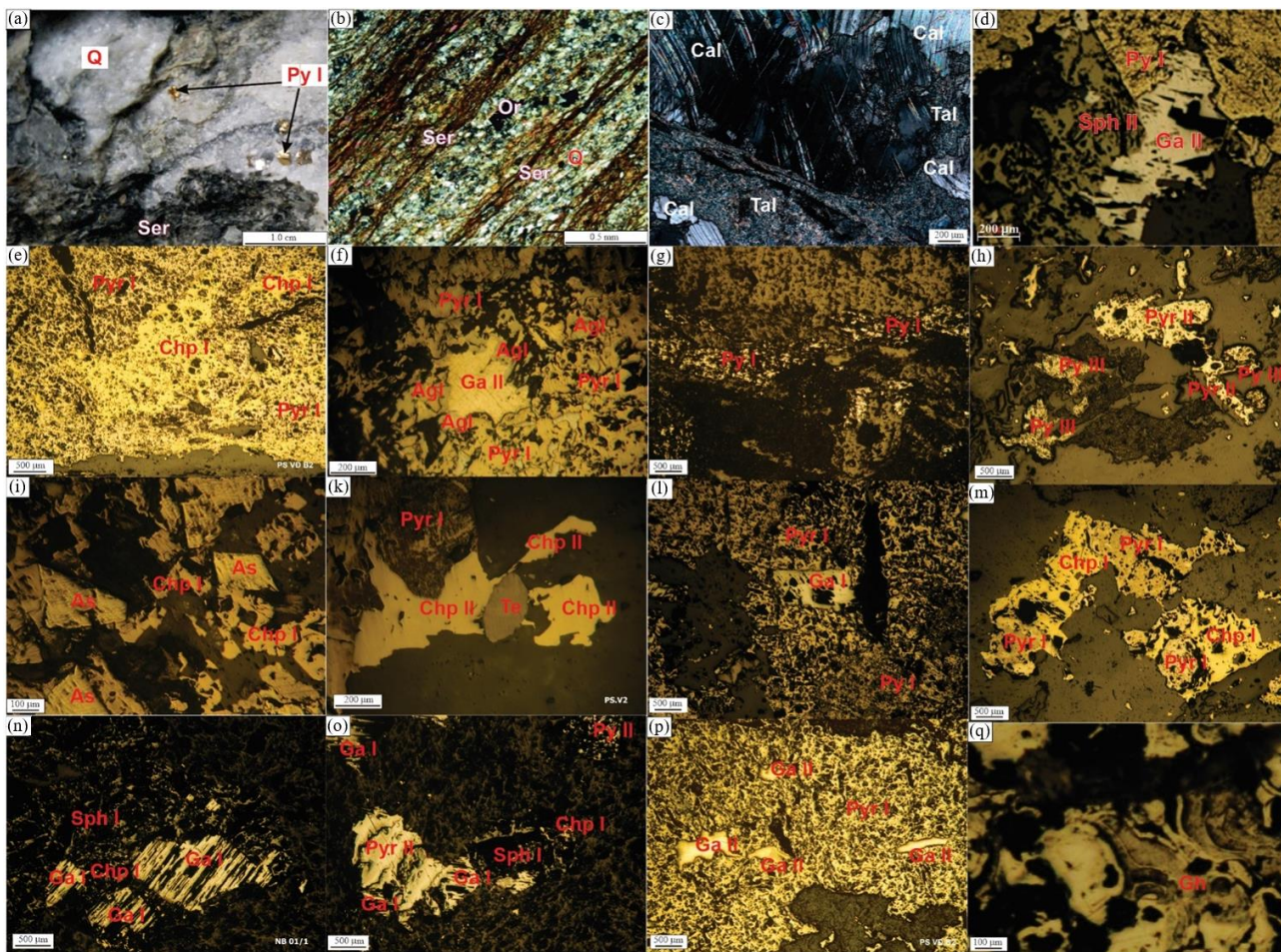

Figure 8. Thin-section and polished-section images of host rock and ore samples from the NPD: (a) pyrite is disseminated within quartz-calcite veins accompanied by sericitic alteration; (b) quartz-sericite schist disseminated sulfide ore is overlays limestone beds containing ore; (c) limestone recrystallized, subjected to calcitization, dolomitization, and talc alteration; (d)-(h) pyrrhotite, pyrite, chalcopyrite in anhedral grains, pyrite in vein disseminations within the rock matrix; (i) arsenopyrite in euhedral grains and chalcopyrite in anhedral grains disseminated on the rock matrix; (k) pyrrhotite, chalcopyrite, and tetrahedrite are disseminated in host rocks; (l) an association of galena, pyrite and pyrrhotite are disseminated in host rocks; (m) pyrrhotite, chalcopyrite in anhedral grains; (n) an association of chalcopyrite, sphalerite, and galena is disseminated in host rocks; (o) an association of galena, sphalerite, chalcopyrite, pyrrhotite, and pyrite are disseminated in host rocks; (p) galena fills in the gaps of pyrrhotite; (q) colloidal goethite. Abbreviations: Cal-Calcite, Do-Dolomite, Tal-Talc, Q-Quartz, Ser-Sericite, Or-Ore, Py-Pyrite, Pyr-Pyrrhotite, Sph-Sphalerite, Ga-Galena, Pyr-Pyrrhotite, As-Arsenopyrite, Te-Tetrahedrite, Agl-Anglesite, Gh-Goethite

Galena II fills the fractures in fractured arsenopyrite grains or occupies the voids in pyrite (Fig. 8d). In some regions of the samples, galena undergoes anglesite alteration, resulting in the formation of thin or thick rims around galena grains or partial replacement (Fig. 8f, p).

Sphalerite is a frequently encountered mineral in the sample set, forming ore mineral assemblages alongside galena within the study area. Similar to galena, the distribution of sphalerite within the analyzed samples is uneven. Sphalerite can be categorized into two generations: Sphalerite I is predominantly observed in anhedral grain form, with grain sizes ranging from 0.01-2 mm, occasionally exceeding 2 mm. Sphalerite I exhibits irregular dispersion within the rock, occasionally forming concentrated clusters or disseminating as veinlets that fill fracture voids while replacing rock-forming minerals. Sphalerite I, galena I, and chalcopyrite I constitute a symbiotic mineral assemblage (Fig. 8n, o). Sphalerite II appears as anhedral grains associated with galena II, quartz, and calcite during the late stage of ore formation, forming cross-cutting veinlets that traverse pre-existing minerals and ores (Fig. 8d).

Pyrite has varying concentrations in most samples, indicating its widespread occurrence throughout the lead-zinc ore formation process. However, the pyrite content in the ore samples varies depending on the stage of ore formation. Pyrite exhibits uneven distribution within the ore veins and the fractured zones closely associated with quartz, calcite, or dolomite. Through analytical results, pyrite can be categorized into distinct generations: Pyrite I appears as anhedral, semi-anhedral, and euhedral grains ranging in size from 0.01-2 mm. Pyrite often aggregates into small nests, occasionally forming large nests and thin veins within the rock matrix (Fig. 8a, d, g, l). Pyrite I fills voids and fractures in the rock, sometimes replacing rock-forming minerals, as evidenced by remnants of quartz and unaltered minerals on the pyrite matrix (Fig. 8h, l). Under mineralogical microscope observation, Pyrite I is observed to be later infiltrated, cemented, and replaced by later sulfide minerals such as sphalerite, galena, and chalcopyrite along fractures. It can be inferred that Pyrite I is the initial ore-forming product formed during the alteration of vein edges under the influence of hydrothermal solutions. Pyrite II appears as anhedral grains with fewer semi-anhedral grains, typically ranging from 0.05 to 0.3 mm. Pyrite II is unevenly dispersed within the rock, forming a typical symbiotic mineral assemblage with sphalerite, galena, and chalcopyrite (Fig. 8o).

Pyrite III exists as anhedral grains with grain sizes ranging from 0.02-0.4 mm, sparsely and unevenly distributed. Occasionally, Pyrite III, along with late-stage minerals such as quartz, calcite, galena II, and sphalerite II, forms cross-cutting veinlets replacing pre-existing mineral assemblages (Fig. 8h). In samples containing pyrite, secondary alteration products result in the formation of goethite, which replaces pyrite through erosive processes. In numerous cases, pyrite is entirely substituted by goethite, assuming a pseudomorphic form resembling pyrite (Fig. 8q). The ore minerals are characterized by both vein and disseminated vein structures, which are typical of all the ore minerals present.

A thick disseminated structure with compact nodules is also observed, resulting from alteration and replacement processes affecting the rock and ore during earlier stages. This process involves the substitution of carbonate minerals, arsenopyrite, pyrite, and pyrrhotite with ore minerals like sphalerite, galena, chalcopyrite, and others during the hydrothermal ore-forming and alteration-exchange stages.

Adhesive structure of secondary minerals in the oxidation zone (goethite): The ore frequently displays plate-like, semi-autonomous, autonomous, and replacement corrosion structures in this context.

3.5.2. Paragenetic sequence

The paragenesis of mineralization at the NPD has been primarily established by analyzing overprinting and cross-cutting relationships among distinct vein sets in the Pb-Zn mineralized zones and microscopic examination of mineral associations. A summarized mineral paragenesis is provided in Figure 9.
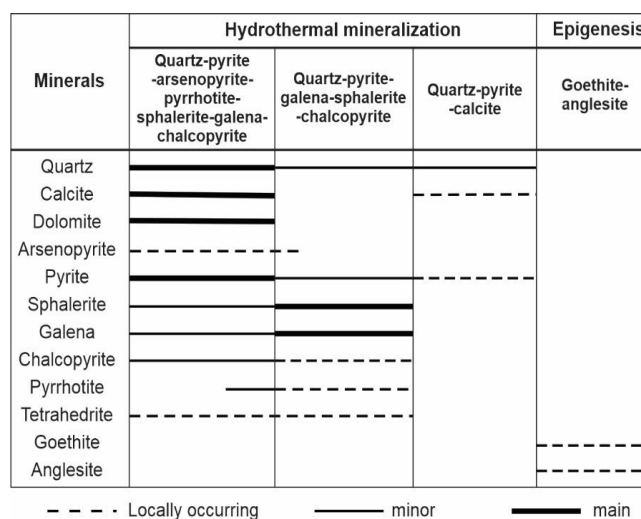
Minerals	Hydrothermal mineralization			Epigenesis
	Quartz-pyrite -arsenopyrite- pyrrhotite- sphalerite-galena- chalcopyrite	Quartz-pyrite- galena-sphalerite -chalcopyrite	Quartz-pyrite -calcite	Goethite- anglesite
Quartz	▬▬▬▬	▬▬▬▬	▬▬▬▬	
Calcite	▬▬▬▬		– – – –	
Dolomite	▬▬▬▬			
Arsenopyrite	– – – –			
Pyrite	▬▬▬▬	▬▬▬▬	– – – –	
Sphalerite		▬▬▬▬		
Galena		▬▬▬▬		
Chalcopyrite		– – – –		
Pyrrhotite	────	– – – –		
Tetrahedrite	– – – –	– – – –		
Goethite				– – – –
Anglesite				– – – –

– – – – Locally occurring　　──── minor　　▬▬▬ main

Figure 9. Mineral paragenesis at the NPD, northeastern Vietnam

Overall, three main stages of mineralization are identified at the NPD, as outlined below:

1. The ore stage (early hydrothermal mineralization) primarily results from the filling of cracks and exchange metamorphism between dolomitized carbonate rocks and hydrothermal fluids, as well as with the ore minerals from the preceding stage. This stage also saw the deposition of sphalerite and galena, albeit in small quantities.

2. The ore stage is the main stage of the NPD. Ore stage assemblage generally includes galena, sphalerite, and pyrite. This stage often overlaps with the ore from the previous stage in space.

3. Post ore stage is marked by small quartz-calcite-pyrite veins cutting through the ore from the previous stage.

3.6. Hydrothermal alteration

The wall-rock alteration consists mainly of quartz, calcite, dolomite, and sericite (Fig. 8b, c). Calcite alteration is widespread in limestone rocks, cracking, fracturing, and significant alteration, particularly near ore veins characterized by fracture zones. Calcite commonly manifests as veins and veinlets, with thicknesses ranging from millimeters to 20mm. Aggregates of calcite are often present in the form of concealed crystalline grains, granular aggregates, and particles of varying sizes (Fig. 8c). Dolomite alteration is conspicuous in limestone zones with a disrupted structure, showcasing porous formations, self-shaped grain structures, partially self-shaped grains, pseudomorphous grains, and

replacements. Certain remnants of calcite may endure depending on the degree of dolomite alteration. In contrast, the alteration can be substantial in other regions, resulting in recrystallized limestone exhibiting dolomite features (Fig. 8e). Quartz alteration occurs subsequently, overlaying the aforementioned alteration processes. This process gives rise to pockets, clusters, vein networks, and quartz mesh structures, occasionally forming scattered crystals through infiltration or coating on a calcite or dolomite background (Fig. 8c). Sericite alteration is evident in the wall rocks surrounding the ore body, where disseminated pyrites are present (Fig. 8a, b).

4. Sampling and analytical methods

4.1. Sampling and petrography observation

As previously elucidated, the mining site manifests two discernible types of ore bodies: the stratiform variant, associated with limestone (TQ.1), and the network-type intersecting limestone (TQ.2). Consequently, a systematic approach is employed in the sampling procedures to ensure an impartial representation of both ore types. Twenty-one sulfide ore samples examined in this investigation were extracted from various levels within the NPD, predominantly from the +230, +210 m (Pu Sap area), and +360, +320 m (Na Bop area) levels (Fig. 3). The sulfide ore and sedimentary carbonates remain in a pristine and unaltered state, sourced from locations specified in section 5. The sulfide ore, sericite, and carbonate samples were crushed to achieve a particle size passing 80 mesh. The sulfides were then concentrated using heavy liquid separation methods to obtain pure, clear sulfide concentrates. These concentrates were carefully handpicked under a binocular microscope, rinsed in deionized water, and ground to a powder (passing 200 mesh) for S-Pb isotope analysis. Additionally, six doubly polished sections of calcite-hosted inclusions from the ore samples were prepared to determine the temperature and salinity of the ore-forming fluid at NPD. Before analysis, micrographs of the samples were taken at various magnifications to assist in the precise selection of measurement points for sulfide mineral analysis.

Two sericite samples for $^{39}Ar/^{40}Ar$ dating were collected from the TQ.1 and TQ.2 ore sublevels, located at 380 and 300 m, respectively, in the Na Bop (NBSr.01) and Pu Sap (PSSr.01) areas, within ore-bearing sulfided shale (Fig. 3). The sericite in these samples displays a syn-tectonic texture associated with sulfide ores (Fig. 5h). Since the sericite minerals are formed in conjunction with lead-zinc mineralization and the absence of organic material in the newly formed sericite within the host shales, it is proposed that sericite formation occurred simultaneously with ore mineralization. Therefore, the $^{39}Ar/^{40}Ar$ data is likely indicative of the timing of the ore-forming event.

4.2. Fluid inclusion study

Fluid inclusion samples used to determine ore-forming temperatures of the NDP are primarily collected from quartz and calcite minerals. However, sampling quartz in the field presents significant challenges due to its brittleness and tendency to fragment quickly. As a result, most fluid inclusion studies are conducted on calcite, a more abundant mineral present in both the early and late stages of hydrothermal activity.

Doubly polished thin sections (approximately 0.20 mm thick) were prepared from six calcite samples for fluid inclusion petrography. The study examined the inclusions' shapes, spatial distribution, genetic and compositional types, and vapor/liquid volume ratios. Six representative samples with abundant fluid inclusions were selected for microthermometric measurements. The inclusion paragenesis was classified according to the criteria outlined by Roedder (1984) [33] and Van den Kerkhof and Hein (2001) [34], categorizing the inclusions as primary, pseudosecondary, and secondary.

Microthermometric analysis of individual fluid inclusions was conducted at the Institute of Geology of Ore Deposits, Petrography, Mineralogy, and Geochemistry. The analysis was performed using a "Linkam" THMSG 600 chamber (England) mounted on an "Olympus BX51" microscope (Japan) with a video camera and control computer. The chemical composition of the fluid captured in the inclusions was determined through measurements of phase transitions during sample heating and cooling. Temperature accuracy was ±0.2°C in the range from -20 to +20°C, with decreasing accuracy at higher and lower temperatures. The dominant salt composition in fluid inclusions was inferred from eutectic melting temperatures [35]. The total salt concentration in two-phase fluid inclusions was estimated from ice melting temperatures using experimental data from the $NaCl – H_2O$ system [36]. Salt concentrations and fluid densities were calculated with the "FLINCOR" program [37].

4.3. Isotope analysis

Createch Testing (Tianjin) Technology Co., Ltd., China, performed sulfur and lead isotope analyses. Grains of sulfide minerals (sphalerite, galena, and pyrite) were carefully hand-picked under a binocular microscope after crushing, cleaning, and sieving through a 200 mesh size, ensuring purity exceeding 95%. Sulfur was released as SO_2 following the method outlined by Fritz et al. (1974) [38], and sulfur isotope analyses were conducted using a MAT-253 mass spectrometer. The results were calibrated against the V-CDT (Vienna standard troilite in Canyon Diablo meteorite) standard, with better analytical precision than ±0.2‰.

In-situ Pb isotopic ratios of galena were measured using a GeoLas HD 193 nm ArF excimer laser coupled with a Neptune Plus MC-ICP-MS. Helium was employed as the carrier gas for the ablation cell, which was subsequently mixed with argon after ablation. Laser ablation spot diameters varied between 44 and 90 μm, depending on the Pb signal intensity. The pulse frequency ranged from 4 to 10 Hz, with a constant laser fluence of approximately 5 J/cm². The accuracy achieved is estimated to be equal to or better than ±0.2‰ for $^{208}Pb/^{204}Pb$, $^{207}Pb/^{204}Pb$, and $^{206}Pb/^{204}Pb$, compared to the solution values obtained by MC-ICP-MS, with a typical precision of 0.4‰ (2σ). Sericite minerals, with a purity exceeding 90%, were selected and subjected to ultrasonic cleaning (Fig. 10).

The cleaned samples were then sealed in quartz bottles and sent to the nuclear reactor at the China Institute of Atomic Energy for neutron irradiation in the "swimming pool pile". The samples underwent staged heating in a graphite furnace, each involving 10 minutes of heating followed by 20 minutes of purification.

Mass spectrometry was analyzed using the multi-receiver noble gas mass spectrometer, Helix MC, with 20 data sets collected for each peak. The data were adjusted to the time-zero value before correcting mass discrimination, atmospheric argon, blanks, and interference isotopes.
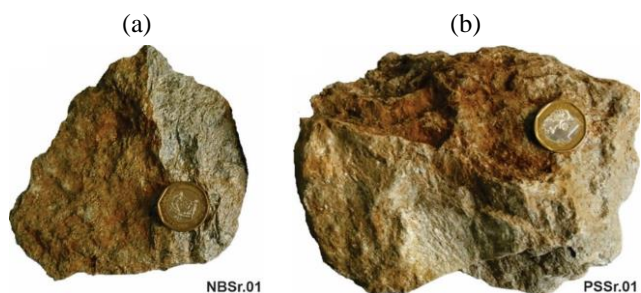
***Figure 10.** Sericite samples are collected from the NPD: (a) NBSr.01 sample from the Na Bop area; (b) PSSr.01 sample from the Pu Sap area*

The interference isotope correction coefficients, determined by analyzing irradiated K_2SO_4 and CaF_2 during neutron irradiation, were as follows:

$(^{36}Ar/^{37}Ar_o)$ Ca = 0.0002398;

$(^{40}Ar/^{39}Ar)$ K = 0.004782;

$(^{39}Ar/^{37}Ar_o)$ Ca = 0.000806.

Additionally, ^{37}Ar was corrected for radioactive decay, using the decay constant for ^{40}K ($\lambda = 5.543 \cdot 10^{-10}$ years^{-1}). The ISOPLOT program calculated the plateau age and positive/negative isochrons, with the reported plateau age error at 1σ.

5. Results

5.1. Isotopic data

5.1.1. Sulfur isotopes

Analytical results of the sulfides are presented in Table 1. This study measured the $\delta^{34}S$ values for twenty-one galena samples, eleven sphalerite samples, and ten pyrite samples from the NPD. The sulfur isotopic compositions for the twenty-one galena samples from the lead-zinc ore ranged from +0.10 to +5.30 ‰, with an average of +3.25‰. For the eleven sphalerite samples, the $\delta^{34}S$ values ranged from +2.50 to +8.49‰, with an average of +6.30‰. The ten pyrite samples had $\delta^{34}S$ values ranging from +4.10 to +5.95‰, averaging +5.04‰. In summary, the sulfide ores from the deposit exhibited $\delta^{34}S$ values ranging from +0.10 to +8.49‰.

5.1.2. Lead isotopes

The Pb isotopic compositions of sulfides from the NPD are summarized in Table 2. Pb isotopic analysis was conducted on eight galena samples, four sphalerite samples, and three pyrite samples. The sulfide ores from the deposit exhibit $^{206}Pb/^{204}Pb$ ratios ranging from 18.451 to 18.651, $^{207}Pb/^{204}Pb$ ratios ranging from 15.685 to 15.836, and $^{208}Pb/^{204}Pb$ ratios ranging from 38.909 to 39.501.

5.1.3. Ar-Ar data

The Ar-Ar analysis results for sericite samples NBSr.01 and PSSr.01 are presented in Table 3. The sericite sample NBSr.01 age spectrum shows a minor gain of radiogenic argon in the twelfth and thirteenth steps. Despite this, the newly formed sericite yielded a $^{39}Ar/^{40}Ar$ plateau age of 237.1 ± 2.3 Ma, based on a 13-step heating spectrum from 500 to 1150°C, with 83.7% of ^{39}Ar released.

The corresponding inverse isochron age is 239.7 ± 2.5 Ma ($n = 6$, MSWD = 1.105), which closely matches the plateau age within the margin of error, confirming the reliability of the data.

***Table 1.** Sulfur-isotope compositions of galena, sphalerite, and pyrite crystals separated from the ore samples of the NPD*

Sample	Location	$\delta^{34}S_{V-CDT}$‰			Ref.
		Galena	Sphalerite	Pyrite	
NB01	Na Bop,	4.77	–	–	
NB02-1	Surface	–	8.49	–	
NB03	Na Bop, 405 m sublevel	1.26	–	–	
NB04	Na Bop, 340 m sublevel	5.13	–	–	
PS01/1		3.45	–	–	
PS01/2		4.25	–	–	
PS01/3-1	Pu Sap,	4.18	–	–	
PS01/3-2	Surface	4.06	–	–	
PS01/4		4.05	–	–	
PS02/1		3.17	–	–	This study
PS02/2	Pu Sap, 315 m sublevel	–	7.53	–	
PS02/3		–	-	4.48	
PS02/4-1	Pu Sap,	–	-	5.86	
PS02/4-2	320 m sublevel	–	-	5.95	
PS03/1		2.94	–	–	
PS03/2	Pu Sap, 300 m sublevel	–	7.04	–	
PS03/3		–	7.37	–	
PS04/1-1	Pu Sap,	–	–	4.63	
PS04/1-2	290 m sublevel	–	–	5.32	
PS04/3	Pu Sap,	3.68	–	–	
PS04/4	305 m sublevel	3.31	–	–	
NB-PS.01	Na Bop,	4.80	6.40	5.20	
NB-PS.02	Surface	5.30	6.80	4.60	
NB-PS.03	Na Bop, 387 m sublevel	4.50	6.70	–	
NB-PS.04	Na Bop, 400 m sublevel	–	–	5.80	
NB-PS.05	Na Bop, 381 m sublevel	–	6.40	4.10	[14]
NB-PS.06	Pu Sap, 324 m sublevel	1.30	–	–	
NB-PS.07	Pu Sap, 302 m sublevel	0.10	2.50	–	
NB-PS.08	Pu Sap, 296 m sublevel	0.70	3.20	–	
PS 08.65a	Pu Sap	2.90	–	–	
KC.1014/1	Na Bop	2.40	–	–	[13]
KC.1039	Pu Sap	2.10	–	–	
SI-0401		–	–	4.50	[39]
SI-0404	Na Bop	–	6.90	–	

***Table 2.** Sulfur-isotope compositions of galena, sphalerite, and pyrite crystals separated from the ore samples of the NPD*

Sample	Minerals	$^{208}Pb/^{204}Pb$	2σ	$^{207}Pb/^{204}Pb$	2σ	$^{206}Pb/^{204}Pb$	2σ	Ref.
NB01/1	Galena	39.17	0.0004	15.74	0.0005	18.57	0.0013	
NB02/1	Galena	39.17	0.0004	15.73	0.0004	18.57	0.0011	This study
PS01/1	Galena	39.16	0.0004	15.73	0.0004	18.55	0.0012	
PS02/1	Galena	39.16	0.0004	15.73	0.0004	18.56	0.0011	
PS03/1	Galena	39.16	0.0005	15.73	0.0005	18.56	0.0014	
NB-PS.01	Galena	39.14	0.0030	15.73	0.0010	18.56	0.0010	
NB-PS.01	Pyrite	39.42	0.0060	15.81	0.0020	18.63	0.0030	
NB-PS.01	Sphalerite	39.32	0.0060	15.78	0.0020	18.61	0.0020	
NB-PS.02	Galena	39.19	0.0020	15.74	0.0010	18.57	0.0010	
NB-PS.02	Pyrite	39.50	0.0060	15.83	0.0020	18.65	0.0020	[14]
NB-PS.02	Sphalerite	39.23	0.0040	15.75	0.0020	18.58	0.0020	
NB-PS.03	Galena	39.35	0.0060	15.79	0.0020	18.61	0.0020	
NB-PS.03	Sphalerite	39.32	0.0040	15.78	0.0020	18.60	0.0020	
NB-PS.04	Pyrite	38.90	0.0050	15.68	0.0020	18.45	0.0020	
NB-PS.05	Sphalerite	39.33	0.0040	15.78	0.0020	18.60	0.0020	

Table 3. Sericite Ar-Ar dating results of the NPD

T (ºC)	$^{40}Ar^*/^{39}Ar$	$^{36}Ar/^{40}Ar$	$^{39}Ar/^{40}Ar$	$^{37}Ar/^{39}Ar$	^{39}Ar in step, %	Atm., %	Age, (Ma)	± 1σ
	Sample NBSr.01, J = 0.01765, λ = 5.543·10⁻¹⁰							
500	7.934	0.045	0.118	0.021	7.6	1.6	236.4	1.7
600	7.991	0.089	0.117	0.063	5.9	2.9	238.0	2.6
650	8.011	0.058	0.118	0.14	5.3	1.9	238.6	2.2
700	8.017	0.084	0.116	0.003	3	2.7	238.8	2.6
750	7.983	0.14	0.117	0.035	5.7	4.3	237.8	1.8
800	8.006	0.068	0.118	0.038	9.4	2.2	238.5	2.8
850	7.967	0.054	0.119	0.01	14.4	1.8	237.4	1.2
900	7.985	0.075	0.117	0.051	8.1	2.4	237.9	1.7
950	7.955	0.085	0.118	0.004	2.1	2.7	237.0	2.6
1000	7.959	0.064	0.119	0.005	13	2.1	237.1	0.9
1050	7.869	0.159	0.116	0.045	2.8	34.9	234.6	1.4
1100	8.222	0.021	0.116	0.015	12.7	0.9	244.5	3.4
1150	8.412	0.439	0.099	0.052	2.4	13.1	249.7	4.8
	Sample PSSr.01, J = 0.01765, λ = 5.543·10⁻¹⁰							
500	7.701	1.012	0.087	0.011	2.5	30.1	229.9	2.7
600	7.768	0.739	0.096	0.036	13.3	22	231.8	3.5
650	7.693	0.462	0.108	0.096	9.1	13.8	229.7	5.6
700	6.921	1.837	0.062	0.022	2.1	54.5	207.9	4.6
750	8.145	0.107	0.115	0.02	9.3	3.3	242.3	1.1
800	8.153	0.087	0.115	0.002	9.6	2.7	242.5	1.8
850	8.092	0.141	0.112	0.014	7.3	4.4	240.8	2.5
950	8.181	0.027	0.117	0.018	11.4	1	243.3	1.3
1050	8.162	0.934	0.084	0.011	7.7	27.8	242.8	2.9
1100	8.158	0.671	0.094	0.006	7.8	20	242.7	2.8

The initial $^{36}Ar/^{40}Ar$ ratio from the isochron plot is 249.7 ± 4.8, indicating no excess argon compared to the atmospheric value of 295.5 [40]. These results suggest that the plateau age of 239.7 ± 2.5 Ma represents the minimum age for the sericite and, by extension, the minimum age for the formation of the NPD. However, the minor gain of radiogenic argon in the twelfth and thirteenth steps may indicate partial resetting of the sericite sample.

Sericite sample PSSr.01 yields a $^{39}Ar/^{40}Ar$ plateau age of 242.6 ± 2.4 Ma from the 5th to 10th heating stages, with 66.3% of the gas released. The corresponding inverse isochron age is 234.1 ± 2.5 Ma ($n = 7$, MSWD = 1.16), with

an initial $^{36}Ar/^{40}Ar$ ratio of 207.9 ± 4.6. These values are nearly identical to the atmospheric value of 295.5, within the margin of analytical error, suggesting that the $^{36}Ar/^{40}Ar$ ratio is reliable. The agreement between the plateau and inverse isochron ages indicates that, after accounting for systematic errors, these ages accurately reflect the timing of metallogenesis. Based on these results, it is inferred that the NPD formed around 242.6 ± 2.4 Ma.

5.2. Fluid inclusions

The mineral hosting the inclusions in this study is calcite. Only type-LV inclusions have been identified within calcite (Fig. 11). A total of 39 inclusions hosted by calcite minerals from the NPD were analyzed, and the details are provided in Table 4. Microthermometric homogenization temperatures ranged from 201 to 245°C, with an average of 223.5°C, predominantly between 200 and 240°C (Table 4).
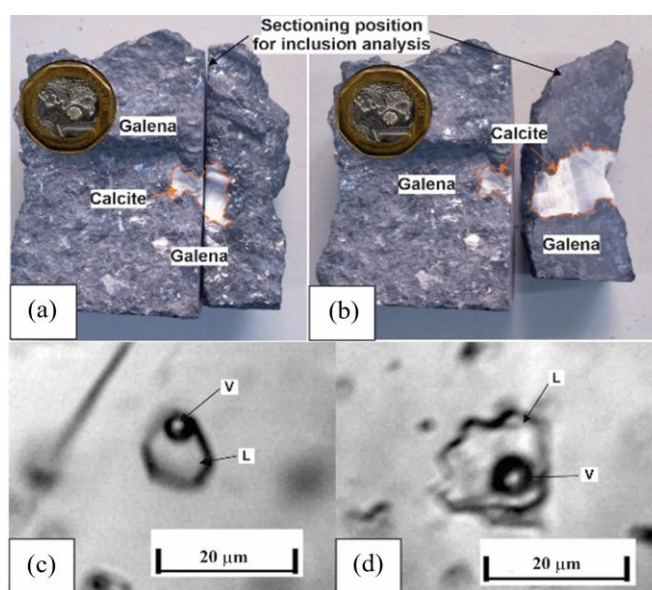

Figure 11. The mineral hosting the inclusions: (a), (b) calcite crystals in a nest-like formation within galena minerals; (c), (d) type-LV inclusions

Table 4. Summary of fluid inclusion data of the NPD

Sample	Host minerals	Number	$T_{m.ice}$ (ºC) (mean)	T_h (ºC) (mean)	Salinity wt% NaCl (mean)	Density (g/cm³) (mean)	Pressure (bar) (mean)	Depth (km) (mean)
NB-I01	Calcite	5	-3.2…-3.6 (-3.4)	234…240 (237)	5.26…5.86 (5.56)	0.862…0.864 (0.863)	628.41…648.26 (638.37)	2.09…2.16 (2.13)
NB-I02	Calcite	8	-2.8…-3.4 (-3.1)	216…245 (231)	4.65…5.56 (5.11)	0.850…0.882 (0.867)	575.84…657.97 (619.30)	1.92…2.19 (2.06)
NB-I03	Calcite	4	-2.8…-3.1 (-3.0)	215…219 (217)	4.65…5.11 (4.96)	0.881…0.887 (0.883)	575.84…586.12 (580.72)	1.92…1.95 (1.94)
PS-I01	Calcite	11	-4.0…-4.7 (-4.3)	215…235 (224)	6.45…7.45 6.88)	0.882…0.898 (0.890)	583.44…641.72 (609.62)	1.94…2.14 (2.03)
PS-I02	Calcite	8	-4.0…-4.8 (-4.4)	205…230 (216)	6.45…7.59 (7.02)	0.889…0.911 (0.901)	557.93…628.54 (588.33)	1.86…2.10 (1.96)
PS-I03	Calcite	3	-4.3…-5.1 (-4.6)	201…215 (208)	6.88…8.00 (7.30)	0.910…0.917 (0.912)	547.05…588.77 (567.47)	1.82…1.96 (1.89)

Note: NB-Na Bop area; PS-Pu Sap area;

a – salinities and density calculated using the method proposed by Bakker (1999, 2018) [41], [42];

b – pressures calculated using the method proposed by Shao and Mei (1986) [43];

c – depths estimated using the method proposed by Sibson (2001, 2004) [44], [45];

$T_{m.ice}$ – final melting temperature of ice;

T_h – homogenization temperature.

The final ice melting temperatures of type-LV inclusions ranged from -2.8 to -5.1°C, corresponding to salinities of 4.65 to 8.00 wt% NaCl, with an average of 6.21 wt% NaCl (Table 4). The densities of the inclusions, calculated using the method of Bakker (1999; 2018) [41], [42], ranged from 0.850 to 0.917 g/cm³ (Table 4). In terms of pressure, the entrapment pressure of these inclusions was estimated to be between 54.7 and 65.8 MPa, using the formula by Shao and Mei (1986) [43] (Table 4).

Three samples were collected for the Na Bop area, each containing 17 two-phase inclusions of vapor-liquid within homogenized calcite. These inclusions exhibited homogenization temperatures between 215 and 245°C, varying salt concentrations from 4.65 to 5.86 wt% NaCl. The ice melting temperatures ranged from -2.8 to -3.5°C, indicating the presence of Na, Mg, and K salts in the solution. The inclusion densities ranged from 0.850 to 0.887 g/cm³. Three samples were collected and analyzed in the Pu Sap area, revealing 22 two-phase vapor-liquid inclusions hosted in homogenized calcite. These inclusions were observed at homogenization temperatures ranging from 201 to 235°C. The salt concentration varied between 6.45 and 8.00 wt% NaCl. The ice melting temperatures of the fluid inclusions ranged from -4.0 to -5.1°C, indicating the presence of Na, Mg, and K salts in the solution. The inclusion densities ranged from 0.882 to 0.917 g/cm³.

6. Discussion

6.1. Sulfur isotopic compositions of sulfide minerals

The primary sulfide minerals in the NPD are sphalerite, galena, and pyrite. The lack of sulfate in the deposit implies that the δ^{34}S values of these sulfide minerals reflect the δ^{34}S values of the fluids that facilitated ore formation [46]. Although pyrite, sphalerite, and galena occur together in the deposit, the formation of galena occurred after sphalerite and pyrite (Fig. 8l), suggesting that these minerals did not form under equilibrium conditions during the ore-forming process. Moreover, the δ^{34}S values of pyrite are lower than those of sphalerite, ranging from 2.50‰ to 8.49%, with values between 4.10‰ and 5.95% (Table 1).

This variation could be attributed to the sulfur not achieving isotopic equilibrium during the hydrothermal system's development or to the depletion of δ^{34}S in the ore-forming fluid due to increasing oxygen fugacity as the fluid evolved [47].

Pyrite found in sulfide minerals at the Pu Sap site displayed δ^{34}S values ranging from 4.48 to 5.95‰, while pyrite from sulfide minerals at the Na Bop site showed δ^{34}S values ranging from 4.10 to 5.80‰ (Table 1). The sulfur isotope compositions from pyrite observed at Pu Sap are comparable to those at Na Bop. This suggests a common or similar sulfur source for the base-metal sulfide deposits within the NPD. However, the narrow range of observed δ^{34}S values (Table 1) indicates that the minerals likely originated from a singular ore-forming source. The δ^{34}S values of the sulfide ore assemblage consistently measured below 10‰, with four galena values showing values below 1.5‰ and approaching 0‰. This indicates a probable link between sulfide mineralization and a deep-seated source, likely associated with magmatic activity in the region (Fig. 12) [48], [49].
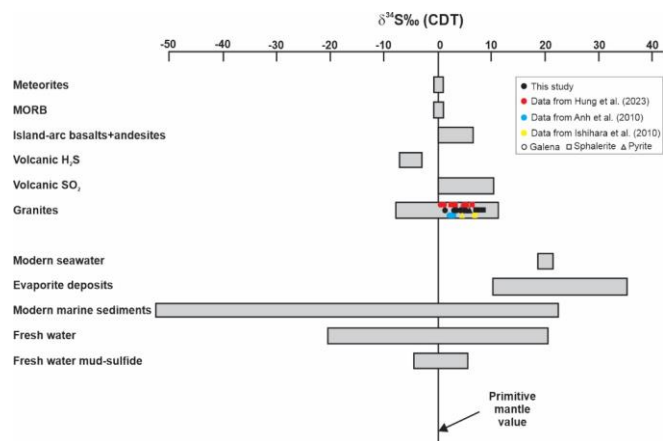

Figure 12. Natural sulfur isotope reservoirs, showing lead-zinc forming material sources in the NPD (data from [50]-[56])

The δ^{34}S isotope values in the sulfur diagram (Fig. 12) provide key insights into the origins of ore-forming sulfur. The data suggest that the sulfur involved in lead-zinc mineralization is likely derived from granite. Several lines of evidence support this interpretation. First, geological observations reveal that sulfide mineralization occurred significantly after forming the Paleozoic host rocks (Figs. 4, 5, 6a, 7c-d), indicating an epigenetic origin. Second, the δ^{34}S values of various sulfide minerals (e.g., pyrite, sphalerite, and galena) from the NPD show a narrow range, which is consistent with sulfur from magmatic fluids [57], [58]. Lastly, Middel-Late Triassic granite massifs, exposed around the peripheral region of the NPD (Figs. 2, 3), suggest that sulfur could have originated from sulfur-rich hydrothermal fluids exsolved from magma chambers that were contemporaneous with the emplacement of these surrounding granite intrusions [9], [10].

Additionally, the δ^{34}S (‰) values for the NPD fall within the range typical of Red-bed and MVT types (Fig. 13). This suggests that the ore deposit is influenced by materials from sedimentary environments, which likely serve as the primary source for the lead-zinc mineralization.
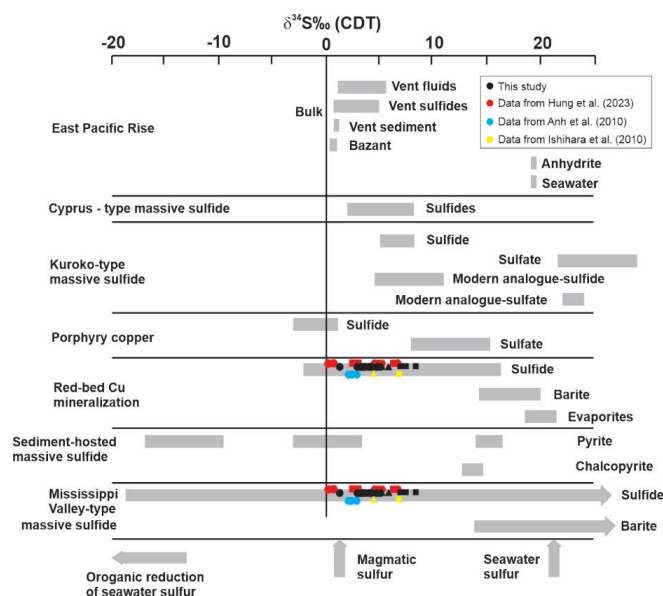

Figure 13. The δ^{34}S values for sulfur-bearing minerals in hydrothermal deposits, showing the lead-zinc deposits of the NPD (data from [59]-[62])

6.2. Pb isotopic composition and metal sources

The observed consistency in Pb isotope compositions suggests the involvement of either a well-mixed multi-source system within extensive hydrothermal processes [63] or a single, uniform source. In the $^{206}Pb/^{204}Pb$ vs. $^{207}Pb/^{204}Pb$ and $^{207}Pb/^{204}Pb$ vs. $^{206}Pb/^{204}Pb$ diagrams (Fig. 14), Pb isotope ratios align closely with the upper crustal curves established by Zartman and Doe (1981) [64]. This pattern indicates that the dominant lead source is the upper crust, with minimal input from juvenile mantle-derived lead. These findings are consistent with Pb isotope studies conducted in the CDO-CDI districts [12], [13].
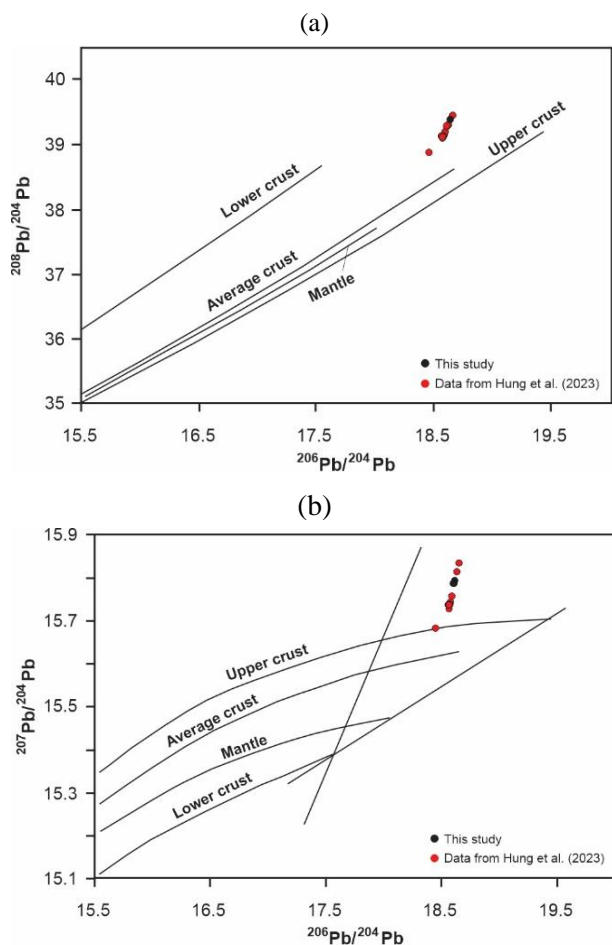
Figure 14. Plot of Pb isotope data from the NPD: (a) $^{208}Pb/^{204}Pb$ vs $^{206}Pb/^{204}Pb$ diagram; (b) $^{207}Pb/^{204}Pb$ vs. $^{206}Pb/^{204}Pb$ diagram; curves of growth trends for Pb isotope ratios are from the plumbotectonic model [64]

The possibility that basement rocks could be the deep-seated source of Pb in the examined deposits is supported by the presence of inherited faults associated with deep-seated fault systems that intersect the Paleozoic rocks (Fig. 3), potentially extending into the basement, such as the NW-SE basement fault. Furthermore, the fact that the deposits are predominantly hosted in Lower Devonian limestones suggests the potential for late-stage remobilization of metals. This idea aligns with similar findings proposed by Hung et al. (2021; 2023) [12], [14] for other Pb-Zn deposits in the CDO-CDI area. These diagrams illustrate the progression of material supply origins, showing a gradual transition toward deeper sources within the upper crust.

Additionally, the schematic by Allegre et al. (1988) [65] delineates the characteristics of material sources contributing to the formation of lead-zinc ores in the NPD, highlighting significant input from enriched mantle sources within the large silicate field of the upper crust (Fig. 15).
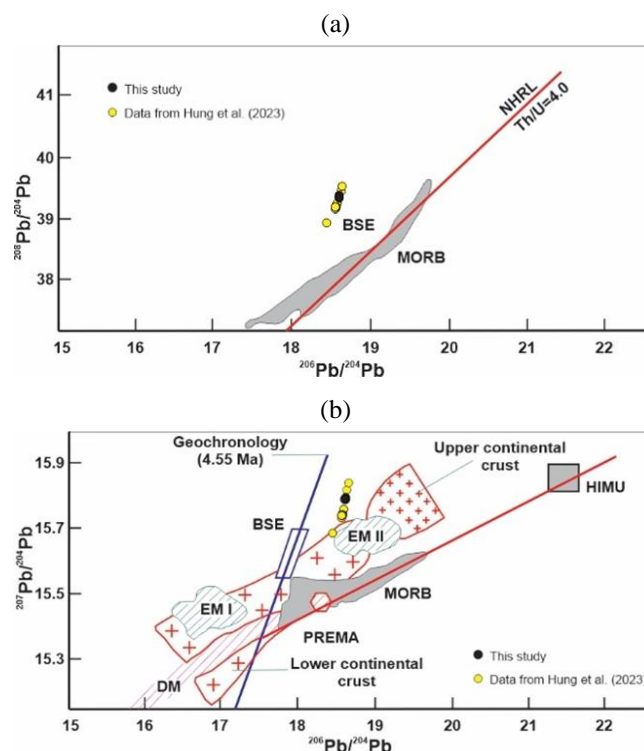

Figure 15. Lead isotope correlation diagrams: (a) the $^{208}Pb/^{204}Pb$ vs. $^{206}Pb/^{204}Pb$ correlation diagram showing the position of the northern hemisphere reference line (NHRL) with $T_h/U = 4.0$; the bulk silicate Earth value (BSE) is from Allegre (et al.1988) [65]; the field of MORB is described with a gray-hatched pattern; (b) the $^{207}Pb/^{204}Pb$ vs. $^{206}Pb/^{204}Pb$ correlation diagram illustrating the position of the northern hemisphere reference line (NHRL), the slope of which has an age significance of 1.77 Ga (HIMU-Mantle with high U/Pb ratio; EM I and EM II-Enriched mantle)

Regarding the correlation of mineralization in the CDI, lead-zinc deposits in the NBD at CDO tend to occur at shallower depths compared to those in the CDI. In CDI, lead-zinc deposits hosted by Devonian sedimentary rocks are typically found at lower crustal levels [4], [12].

6.3. Timing of Pb-Zn mineralization

The $^{40}Ar/^{39}Ar$ geochronological technique offers significant potential for mineral deposit studies. This method delivers precise age estimates of mineral deposits but also aids in determining the duration and number of mineralization phases. By analyzing the distribution of argon within the minerals using the age spectrum approach, insights can be gained into the extent of alteration in preexisting minerals caused by the mineralization process [66].

The timing of mineralization is constrained by:

1) the Pb-Zn ore occurs in stratiform, as cross-cutting veins within lower Devonian limestone;

2) a syn-tectonic texture between the sericite and lead-zinc minerals present in the NPD;

3) using Ar-Ar isotopic dating of sericite minerals to determine the formation age of lead-zinc ores. From the Ar-Ar isotopic data, we obtained ages of sericite minerals around 237.1 ± 2.3 Ma to 242.6 ± 2.4 Ma, corresponding to the Middle-Late Triassic (Table 3, Fig. 16).

A thermal event in northeastern Vietnam, contemporaneous with the emplacement of the Phia Bioc granites around 240-250 Ma, may have contributed to the region's geological evolution. During the Indosinian orogeny, Pb and Zn metal sources, derived initially from granitic massifs in the upper crust, became isolated.

Later, tectonic activity reactivated these metal sources, facilitating the transport of Pb and Zn along NW-SE fracture systems [47]. This process enabled the migration of mineralizing fluids, leading to the eventual formation of the NPD.

(a)   (b)

(c)   (d)
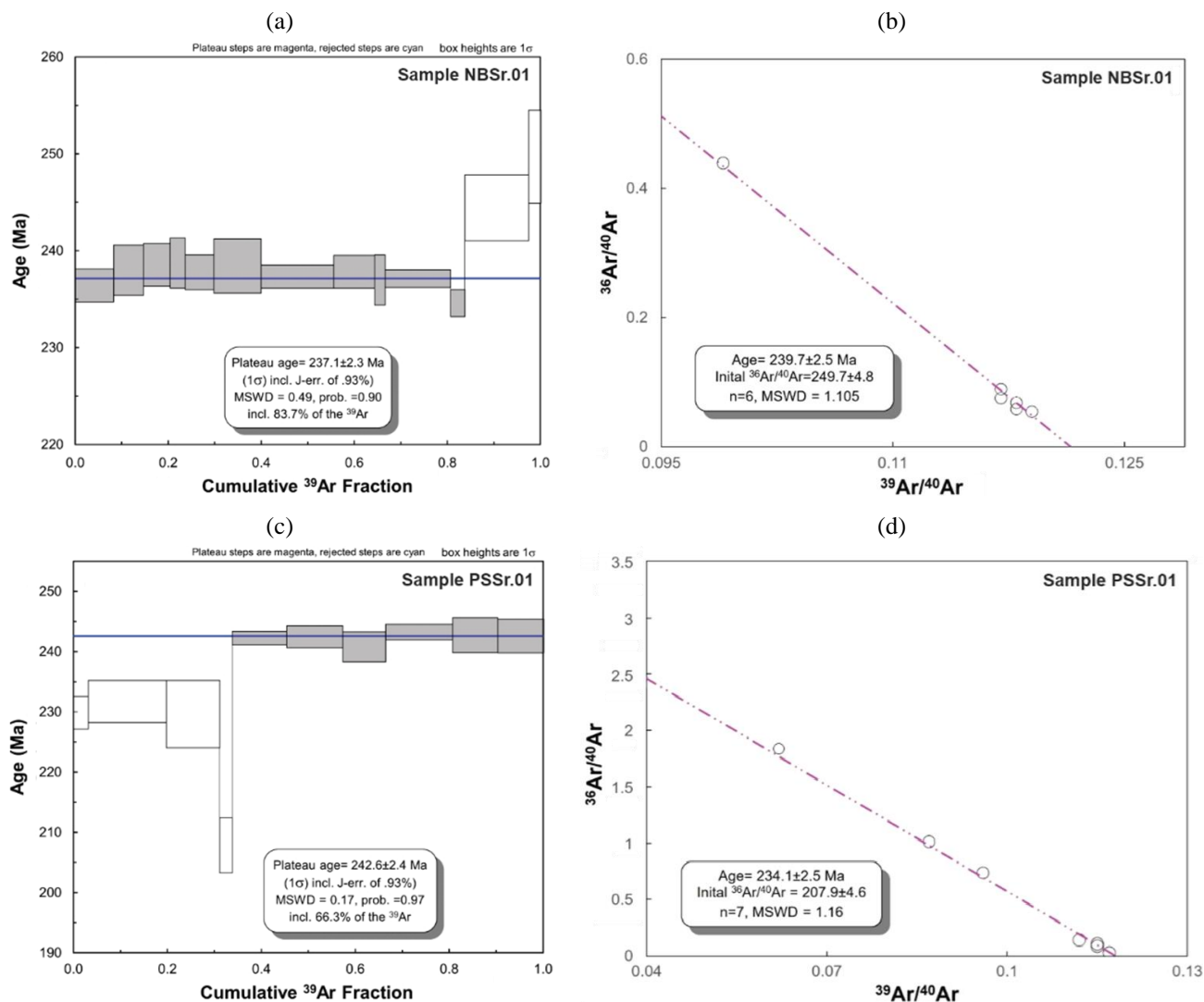
Figure 16. ^{40}Ar-^{39}Ar ages of sericite from the NPD: (a), (c) step heating spectrums; (b), (d) inverse isochrons

6.4. Ore-forming fluid

The microthermometric data suggest that the ore-forming fluid was characterized by moderate temperature and salinity conditions (Table 4). Homogenization temperatures of fluid inclusions in the NPD span from 201 to 245°C, with salinities ranging from 4.65 to 8.00 wt% NaCl, and pressures between 54.7 and 65.8 MPa, corresponding to depths of 1.82 to 2.19 km (Table 4; Fig. 17). These findings imply that the lead-zinc mineralization likely occurred during the epithermal stage.

Based on the temperature-salinity diagram of fluid inclusions, the NPD plots within the epithermal lead-zinc deposits and massive sulfide deposits (Fig. 18). Moreover, the fluid inclusion data of the NPD is very similar to that of polymetallic hydrothermal deposits [67].

6.5. Genesis of the NPD

A comparison of the characteristics of the NBD with established SEDEX and MVT ore deposit models worldwide reveals that it needs to fully align with the specific features of both models (Table 5). However, the available data strongly suggests a magmatic-hydrothermal origin for the NBD. The presence of deep-sourced magmatic sulfur isotopes, upper crustal lead signatures, and fluid inclusion evidence collectively indicate the involvement of magmatic fluids that ascended along fault zones, subsequently mixing with crustal and/or meteoric waters to precipitate lead-zinc ores in a carbonate host. Additionally, the syntectonic textures observed between sericite and sulfide ore minerals imply that mineralization occurred during a phase of tectonic activity, likely associated with magmatic intrusions and hydrothermal fluid flow during the Middle-Late Triassic.
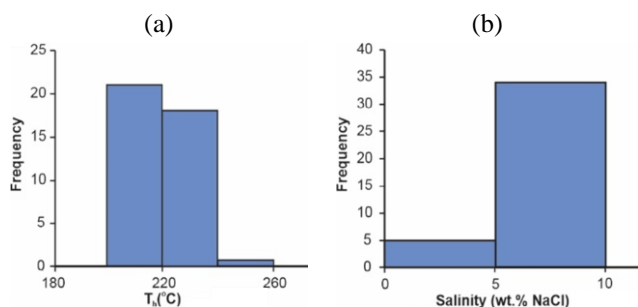
Figure 17. Histogram of temperature and salinity distributions in fluid inclusions from the NPD: (a) homogeneous temperature; (b) salinity distribution
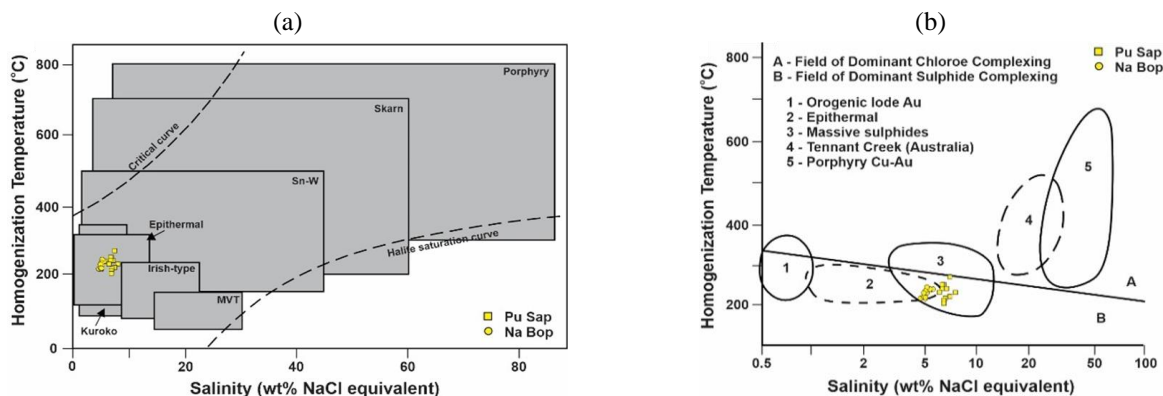
Moreover, the proximity of the Middle-Late Triassic Cho Don granitic massif to the NPD suggests a potential genetic relationship between the two. This indicates that the formation of the NPD may have been influenced by tectonic processes associated with the Cho Don granitic massif. Specifically, the Phia Bioc granite complex, which formed in a post-collision setting (e.g., [29]), indicates that the deposit likely developed as a result of the collision between the Sibumasu and Indochina blocks during the closure of the Paleo-Tethys Ocean (Fig. 19).
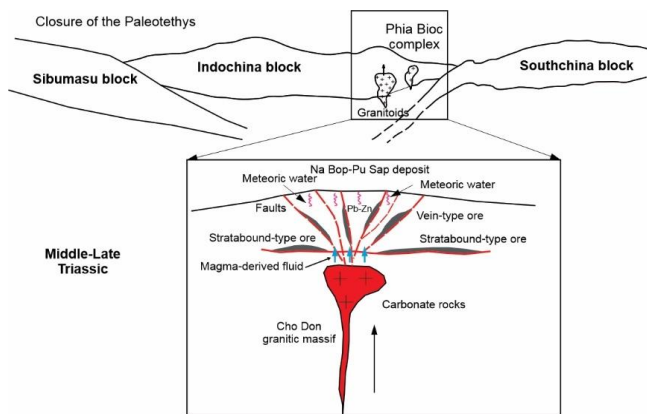

Figure 18. Classification of mineral deposits based on fluid inclusion temperature and salinity: (a) hydrothermal deposits; (b) field of dominant chlorite/sulfide complexing (after [68])

Table 5. Comparison between NPD, SEDEX, and MVT deposits

Characteristic	NPD deposit	SEDEX deposits	MVT deposits
Size and grade of individual deposits	Totaly 32 Mt ore; Pb + Zn 6 to 19 %, no significant Cu; Bimodal Zn:(Zn + Pb) distribution	Mostly > 30 Mt, many contain > 100 Mt ore; Commonly Cu + Zn + Pb >10%, Cu< 1%; Bimodal Zn:(Zn + Pb) distribution	Mostly < 1 Mt. ore; Zn + Pb 3 to 10 %, typically no Cu; Bimodal Zn:(Zn + Pb) distribution
Metals recovered or concentrated.	Major: Pb, Zn Minor: Ag, Cd	Major: Zn, Pb (+Cu in some deposits) Minor: Cu, Ag	Major: Zn, Pb Minor: Cd, Ag, Ge
Characteristic ore-gangue assemblage	Quartz + ars + po + cp + sp + ga + py	py/po + sp + ga ± cp ± barite	sp ± ga ± fluorite ± barite ±py/ms ± calcite/dolomite ±chert
Typical host rock sequence	Limestones, dolomites, and sericite schists of the Cocxo formation	Shallow- to deep-water marine clastics and carbonates, interspersed with thin bands of tuffite. Associations with evaporites and redbeds are not characteristic	Shallow-water, platform-associated carbonate rocks, such as limestones and dolomitized limestones, host the ores predominantly in dolostone rather than in the limestone itself
Age of host rocks	Early Devonian	Early Proterozoic to the Late Paleozoic, with a dominant presence in the Early to Middle Proterozoic	Primarily Paleozoic, spanning from the Early Proterozoic to the Jurassic
Nature of mineralization	Conformable, stacked lenses of stratiform massive sulfide (syngenetic), which are underlain by a zone of discordant, stockwork mineralization (epigenetic)	Conformable, stacked lenses of stratiform massive sulfide (syngenetic), which are underlain by a zone of discordant mineralization (epigenetic)	Strata-bound, massive to disseminated, cavity-filling mineralization, most commonly cementing breccia fragments; minor replacement mineralization
Hydrothermal alteration	Qualification, calcification, dolomitization, sericitization, and fracturing in the footwall rocks	Footwall alteration ranges from significant to subtle or may even be absent in some instances.	Dolomitization (potentially not directly related to ore fluids), silicification, and enhanced illite crystallinity
Metal zoning	No characteristic zoning pattern	Cu => Zn + Pb => barite	Absence of a distinct zoning pattern
Ore-forming fluids	Moderate salinity (4.65 – 8.00 wt% NaCl equiv.), moderate temperature (201-245°C)	High salinity (10 - 30 wt % NaCl equiv.), moderate temperature (100° – 300°C)	High salinity (> 15 wt% NaCl equivalent) and low temperature (typically 100-150°C)
Controls of mineralization	Carbonates, faults	Synsedimentary faulting, anoxic conditions, and the presence of appropriate source rocks for metal accumulation. Characterize rift basins	Platform carbonates, breccia bodies, facies transitions, basement highs and pinch-outs, faults, and limestone-dolostone interfaces
Genetic model	Magmatic-hydrothermal type	Synsedimentary to syn-diagenetic mineralization originating from basinal brines	Epigenetic mineralization resulting from basinal brines
Tectonic setting	Proposal for a post-collision setting	Mostly intracontinental rifts	Foreland thrust belts, intracratonic sedimentary basins (edges)

Abbreviations: ars – arsenopyrite; py – pyrite; ms – marcasite; po – pyrrhotite; sp – sphalerite; ga – galena; cp – chalcopyrite; bn – bornite; Mt – million tonnes

Figure 19. *A genetic model of the NPD in the Cho Don area during the Middle-Late Triassic*

7. Conclusions

The NPD in the CDO area of northeastern Vietnam has been extensively analyzed using geological, mineralogical, Pb, S, and Ar-Ar isotope data and fluid inclusions to explore the origins of lead-zinc deposits and their associated ore-forming materials. The findings from this investigation yield several significant conclusions.

Firstly, examination of the geological profile both on the surface and beneath the furnace indicates that the lead-zinc ore bodies at the NBD exhibit a strata-bound and vein-like structure characterized by lenses. Within these formations, vein-type ores develop along fracture planes trending NW-SE, with primary ore minerals identified as galena, sphalerite, pyrrhotite, pyrite, arsenopyrite, and pyrrhotite. The ore displays disseminated structures and an anhedral to semi-euhedral textural morphology.

Secondly, analysis of $\delta^{34}S$ values from galena, sphalerite, and pyrite samples suggests a probable connection between sulfide mineralization and a deep-seated source, likely associated with magmatic activity in the region. These $\delta^{34}S$ values fall within the Red-bed and MVT field types, indicating that they constitute the primary reservoir for lead-zinc mineralization.

Thirdly, lead isotope analysis reveals that the ore formations of the NPD originate from material sources within the large silicate field of the upper crust, with a significant contribution from mantle sources. However, the material sources involved in the NPD are closer to rich mantle sources than those in the CDO area.

Fourthly, the sericite Ar-Ar dating results indicate that lead-zinc mineralization occurred between 237.1 ± 2.3 Ma and 242.6 ± 2.4 Ma, corresponding to the Middle-Late Triassic. These findings suggest that the ore materials are likely related to the Phia Bioc granitic complex, particularly the Cho Don granitic massif near the NPD.

Furthermore, micro thermometric data indicate that the ore-forming fluid exhibited moderate temperature (201-245°C) and salinity under pressures ranging from 54.7 to 65.80 MPa, corresponding to depths of 1.82-2.19 km. This suggests that the lead-zinc mineralization belongs to the epithermal origin. Eventually, intrusive activity diminished, and hydrothermal activity was driven by hydrostatic pressure dominated by meteoric water.

Lastly, the NPD does not fully conform to the specific characteristics of SEDEX or MVT ore deposit types. However, it exhibits features indicative of a magmatic-hydrothermal type, likely resulting from the collision between the Sibumasu and Indochina blocks during the Middle-Late Triassic.

Conflicts of interests

The authors declare no conflict of interest.

Data availability statement

The original contributions presented in the study are included in the article, further inquiries can be directed to the corresponding author.

References

[1] Sangster, D.F. (1996). *Carbonate-hosted lead-zinc deposits: 75th anniversary volume*. Littleton, United States: Society of Economic Geologists, 654 p. https://doi.org/10.5382/SP.04

[2] Tri, T.V., & Khuc, V. (2011). *Geology and earth resources of Vietnam*. Hanoi, Vietnam: Publishing House for Science and Technology, 634 p.

[3] Hoa, T.T., Anh, T.T., Phuong, N.T., Izokh, A.E., Polyakov, G.V., Balykin, P.A., Ching-Ying Lan, Thanh, H.H., Nien, B.A., & Dung, P.T. (2004). Gabbro-syenite associations of East Bac Bo structures: evidence of intra-plate magmatism? *Journal of Geology, Series B, 23*, 12-25.

[4] Binh, D.Q., Cuong, D.Q., Chinh, K.T., Hung, N.M., & Que, N.T. (2005). *Report on prospective results of lead-zinc, gold, and accompanying minerals of the Phia Da-Na Cang area, Cao Bang-Bac Kan provinces*. Hanoi, Vietnam: Vietnam Institute of Geosciences and Mineral Resources, 193 p.

[5] Hoa, T.T., Izokh, A.E., Polyakov, G.V., Borisenko, A.S., Anh, T.T., Balykin, P.A., Phuong, N.T., Rudnev, S.N., Van, V.V., & Nien, B.A. (2008). Permo-Triassic magmatism and metallogeny of Northern Vietnam in relation to the Emeishan plume. *Russian Geology and Geophysics, 49*, 480-491. https://doi.org/10.1016/j.rgg.2008.06.005

[6] Binh, D.Q., Cuong, D.Q., Dong, N.C., De, P.Q., Linh, N.T.H., Que, N.T., & San, V.T. (2010). *Report on prospective results of copper, lead-zinc, and accompanying minerals of the Quang Ba-Pac Nam area, Ha Giang province*. Hanoi, Vietnam: Vietnam Institute of Geosciences and Mineral Resources, 179 p.

[7] Hung, K.T., Sang, P.N., Phuong, N., Linh, V.T., & Sang, B.V. (2020). Statistical evaluation of the geochemical data for prospecting polymetallic mineralization in the Suoi Thau – Sang Than region, Northeast Vietnam. *Geology, Geophysics and Environment, 6*(4), 285-299. https://doi.org/10.7494/geol.2020.46.4.285

[8] Vinh, N.K. (1982). Radioactive age and metallogenic specialization of Phia Bioc granite complex based on geochemical and lead isotope data. *Journal of Geology, 154*, 23-25.

[9] Niem, N.V. (2013). *Establishing a scientific basis for constructing models of lead-zinc ore genesis in Northern Vietnam*. Project. Hanoi, Vietnam: Ministry of Natural Resources and Environment.

[10] Hoa, T.T., Anh, T.T., Dung, P.T., Hung, T.Q., Nien, B.A, Hieu, T.V., & Can, P.N. (2010). By-products in lead-zinc and copper ores of Northeast Vietnam. *Journal of Earth Sciences, 32*(4), 289-298.

[11] Tung, T.T., Tuan, L.C., Binh, D.Q., Quang, N.T., & Giang, N.T. (2024). Sedimentary exhalative Pb-Zn deposit model of the Ban Lin – Phia Dam ore range, Vietnam. *Mining of Mineral Deposits, 18*(3), 25-32. https://doi.org/10.33271/mining18.03.025

[12] Hung, K.T., Tung, T.D., Binh, D.Q., Sang, P.N., Cuc, N.T., Linh, N.T.H., & Tin, Q.D. (2021). Sulfur and lead isotope geochemical characteristics of Pb-Zn deposits in the Khau Loc zone, northeastern Vietnam, and their significance. *Journal of Geology, Geophysics and Environment, 47*(3), 143-157. https://doi.org/10.7494/geol.2021.47.3.143

[13] Anh, T.T., Dung, P.T., Hoa, T.T., Nien, B.A., Hung, T.Q., Phuong, N.T., Anh, P.L., Can, P.N., Ly, V.H., Hieu, T.V., Lam, T.H., Hang, H.V., & Thuong, V.T. (2010). *Enhancing mineral extraction efficiency and en-*

vironmental protection: Investigating associated components in basic metal and rare earth mineral deposits in northern Vietnam. State Science & Technology Programme, code KC.08.24/06-10. Hanoi, Vietnam: 459 p.

[14] Hung, K.T., Truong, L.X., Awadh, S.M., Thang, T.V., Dac, N.X., Du, N.K. (2023). Geology, Pb and S Isotope Geochemistry, and Genesis of the NPD in the Cho Don area, Northeastern Vietnam. *Iraqi Geological Journal, 56*(2), 164-177. https://doi.org/10.46717/igj.56.2C.13ms-2023-9-19

[15] Dovjikov, A.E., My, B.P., Vasilevskaya, E.D., Zhamoida, A.I., Ivanov, G.V., Izokh, E.P., Huu, L.D., Mareichev, A.M., Tien, N.V., Tri, N.T., Luong, T.D., Quang, P.V., & Long, P.D. (1965). *Geology of Northern Vietnam*. Hanoi, Vietnam: Nauka i Tekhnika.

[16] Tri, T.V., Uy, N.D., Hiep, N., Hoai, H.D., Quy, H.H., Sang, N.T., San, N., Thanh, L., Thuan, C.X., Thuc, P.V., & Tuyet, D. (1977). A tectonic sketch of the northern Vietnam at scale of 1:1000000. *Journal of Geology, 123*, 1-2.

[17] Thanh, N.V., An, N.P., Duan, P.V., Hoe, P.H., & Son, V.M. (2002). New data on the Rb-Sr isotopic age of granitoids from the Song Hin complex. *Journal of Geology, Series B, 19-20*, 103-107.

[18] Anh, P.L., & Hang, H.V. (2005). The Late Permian age of S-granite from Tam Tao massif. *Journal of Earth Sciences, 27*(2), 115-124.

[19] Izokh, A.E., Polyakov, G.V., Hoa, T.T., Balykin, P.A., & Phuong, N.T. (2005). Permian-Triassic ultramafic-mafic magmatism of northern Vietnam and southern China as expression of plume magmatism. *Russian Geology and Geophysics, 46*(9), 922-932.

[20] Polyakov, G.V., Shelepaev, R.A., Hoa, T.T., Izokh, A.E., Balykin, P.A., Phuong, N.T., Hung, T.Q., & Nien, B.A. (2009). The Nui Chua layered peridotite-gabbro complex as manifestation of Permo-Triassic mantle plume in northern Vietnam. *Russian Geology and Geophysics, 50*(6), 501-516. https://doi.org/10.1016/j.rgg.2008.10.002

[21] Dobretsov, N.L., Borisenko, A.S., Izokh, A.E., & Zhmodik, S.M. (2010). A thermochemical model of Eurasian Permo-Triassic mantle plumes as a basis for prediction and exploration for Cu-Ni-PGE and rare-metal ore deposits. *Russian Geology and Geophysics, 51*(9), 903-924. https://doi.org/10.1016/j.rgg.2010.08.002

[22] Lepvrier, C., Faure, M., Voung, N.V., Tich, V.V., Lin, W., Thang, T.T., & Phuong, T.H. (2011). North-directed Triassic nappes in Northeastern Vietnam (East Bac Bo). *Journal of Asian Earth Sciences, 41*, 56-68. https://doi.org/10.1016/j.jseaes.2011.01.002

[23] Nevolko, P.A., Dung, P.T., Fominykh, P.A., Hoa, T.T., Anh, T.T., & Phuong, N.T. (2019). Origin of the intrusion-related Lang Vai gold-antimony district (Northeastern Vietnam): Constraints from fluid inclusions study and C-O-S-Pb isotope systematics. *Ore Geology Reviews, 104*, 114-13. https://doi.org/10.1016/j.oregeorev.2018.10.019

[24] Truong, N.X. (1995). *Research on prospecting and estimation results of Pb-Zn ore mineralization in Na Bop deposit, Cho Don area, Bac Kan province*. Hanoi, Vietnam: Center for Information and Archives of Geology.

[25] Quoc, N.K. (2000). *Report on results of geological mapping and mineral investigation of Bac Kan sheet at 1:200000 scale*. Hanoi, Vietnam: Geological Department of Vietnam.

[26] Bac, D.T. (2011). *Research on characteristics and distribution regularities of lead-zinc metallogenic formations in the Viet Bac area, Northern Vietnam*. PhD Thesis. Hanoi, Vietnam: Hanoi University of Mining and Geology.

[27] Sang, B.V. (2010). *Report on lead-zinc ore exploration in the Na Bop-Pu Sap area, Chon Don district, Bac Kan province*. Hanoi, Vietnam: General Department of Geology and Minerals of Vietnam.

[28] Lepvrier, C., Maluski, H., Tich, V.V., Leyreloup, A., Phan, V.T., & Nguyen, V.V. (2004). The Early Triassic Indosinian orogeny in Vietnam (Truong Son Belt and Kon Tum Massif): Implications for the geodynamic evolution of Indochina. *Tectonophysics, 393*, 87-118. https://doi.org/10.1016/j.tecto.2004.07.030

[29] Hung, K.T. (2010). Overview of magmatism in northwestern Vietnam. *Annales Societatis Geologorum Poloniae, 80*(2), 185-226.

[30] Shellnutt, J.G., Jahn, B.-M., & Zhou, M.-F. (2011). Crustal-derived granites in the Panzhihua region, SW China: Implications for felsic magmatism in the Emeishan Large Igneous province. *Lithos, 123*, 145-157. https://doi.org/10.1016/j.lithos.2010.10.016

[31] Roger, F., Maluski, H., Lepvrier, C., Van, T.V., & Paquette, J.-L. (2012). LA-ICPMS zircons U/Pb dating of Permo-Triassic and Cretaceous magmatisms in Northern Vietnam – Geodynamical implications. *Journal of Asian Earth Sciences, 48*, 72-82. https://doi.org/10.1016/j.jseaes.2011.12.012

[32] Wang, C.Y., Zhou, M.F., & Qi, L. (2007). Permian flood basalts and mafic intrusions in the Jinping (SW China)-Song Da (northern Vietnam) district: Mantle sources, crustal contamination and sulfide segregation. *Chemical Geology, 243* (3-4), 317-343. https://doi.org/10.1016/j.chemgeo.2007.05.017

[33] Roedder, E. (1984). Fluid inclusions. *Reviews in Mineralogy, 12*, 1-644. https://doi.org/10.1515/9781501508271

[34] Van den Kerkhof, A.M., & Hein, U.F. (2001). Fluid inclusion petrography. *Lithos, 55*, 27-47. https://doi.org/10.1016/S0024-4937(00)00037-2

[35] Borisenko, A.S. (1977). The study of the salt composition of solutions of gas-liquid inclusions in minerals by cryometry. *Geology and Geophysics, 8*, 16-27.

[36] Bodnar, R.J., & Vityk, M.O. (1994). Interpretation of microthermometric data for H_2O-NaCl fluid inclusions. *Fluid Inclusions in Minerals: Methods and Application*, 117-130.

[37] Brown, P.E. (1989). FLINCOR: A microcomputer program for the reduction and investigation of fluid inclusion data. *American Mineralogist, 74*, 1390-1393.

[38] Fritz, P., Drimmie, R.J., & Nowicki, V.K. (1974). Preparation of sulfur dioxide for mass spectrometer analyses by combustion of sulfides with copper oxide. *Analytical Chemistry, 46*(1), 164-166. https://doi.org/10.1021/ac60337a044

[39] Ishihara, S., Anh, T.T., Yasushi, W., & Hoa, T.T. (2010). Chemical characteristics of lead-zinc ores from North Vietnam, with a special attention to the in contents. *Bulletin of the Geological Survey of Japan, 61*, 307-23. https://doi.org/10.9795/bullgsj.61.307

[40] Steiger, R.H., & Jager, E. (1977). Subcommission on geochronology: convention on the use of decay constants in geo- and cosmochronology. *Earth and Planetary Science Letters, 36*(3), 359-362. https://doi.org/10.1016/0012-821X(77)90060-7

[41] Bakker, R.J. (1999). *Optimal interpretation of microthermometrical data from fluid inclusions: Thermodynamic modelling and computer programming*. Habilitation Thesis. Heidelberg, Germany: University Heidelberg, 50 p.

[42] Bakker, R.J. (2018). AqSo_NaCl: Computer program to calculate P-T-V-X properties in the H_2O-NaCl fluid system applied to fluid inclusion research and pore fluid calculation. *Computers and Geosciences, 115*, 122-133. https://doi.org/10.1016/j.cageo. 2018.03.003

[43] Shao, J.L., & Mei, J.M. (1986). On the study of typomorphic characteristics of mineral inclusion in the gold deposit from volcanic terrain in Zhejiang and its genetic and prospecting significance. *Mineral Rocks, 3*, 103-111.

[44] Sibson, R.H. (2001). Seismogenic framework for hydrothermal transport and ore deposition. *Reviews in Economic Geology, 14*, 25-50. https://doi.org/10.5382/Rev.14.02

[45] Sibson, R.H. (2004). Controls on maximum fluid overpressure defining conditions for mesozonal mineralisation. *Journal of Structural Geology, 26*, 1127-1136. https://doi.org/10.1016/j.jsg.2003.11.003

[46] Ohmoto, H. (1972). Systematics of sulfur and carbon isotopes in hydrothermal ore deposits. *Economic Geology, 67*, 551-579. https://doi.org/10.2113/gsecongeo.67.5.551

[47] Pirajno, F. (2009). *Hydrothermal processes and mineral systems*. Dordrecht, the Netherlands: Springer, 1249 p. https://doi.org/10.1007/978-1-4020-8613-7

[48] Duan, J., Tang, J., & Lin, B. (2016). Zinc and lead isotope signatures of the Zhaxikang Pb-Zn deposit, South Tibet: Implications for the source of the ore-forming metals. *Ore Geology Reviews, 78*, 58-68. https://doi.org/10.1016/j.oregeorev.2016.03.019

[49] Gill, S., Piercey, S., Layne, G.D., & Piercey, G.D. (2019). Sulphur and lead isotope geochemistry of sulphide minerals from the Zn-Pb-Cu-Ag-Au Lemarchant volcanogenic massive sulphide (VMS) deposit, Newfoundland, Canada. *Ore Geology Reviews, 104*, 422-435. https://doi.org/10.1016/j.oregeorev.2018.11.008

[50] Coleman, M.L. (1977). Sulphur isotopes in petrology. *Journal of the Geological Society, 133*, 593-608. https://doi.org/10.1144/gsjgs.133.6.0593

[51] Claypool, G.E., Helser, W.T., Kaplan, I.R., Sakai, H., & Zak, I. (1980). The age curves of sulfur and oxygen isotopes in marine sulfate and their mutual interpretation. *Chemical Geology, 28*, 199-260. https://doi.org/10.1016/0009-2541(80)90047-9

[52] Chambers, L.A. (1982). Sulfur isotope study of a modem intertidal environment and the interpretation of ancient sulfides. *Geochimica et Cosmochimica Acta, 46*, 721-728. https://doi.org/10.1016/0016-7037(82)90023-0

[53] Sakai, H., Casadevall, T.J., & Moore, J.G. (1982). Chemistry and isotope ratios of sulfur in basalts and volcanic gases at Kilauea volcano, Hawaii. *Geochimica et Cosmochimica Acta, 46*, 729-738. https://doi.org/10.1016/0016-7037(82)90024-2

[54] Kerridge, J.F., Haymon, R.M., & Kastner, M. (1983). Sulfur isotope systematics at the 21ºN site, East Pacific Rise. *Earth and Planetary Science Letters, 66*, 91-100. https://doi.org/10.1016/0012-821X(83)90128-1

[55] Ueda, A., & Sakai, H. (1984). Sulfur isotope study of Quaternary volcanic rocks from the Japanese islands arc. *Geochimica et Cosmochimica Acta, 48*, 1837-1848. https://doi.org/10.1016/0016-7037(84)90037-1

[56] Chaussidon, M., Albarede, F., & Sheppard, S.M.F. (1989). Sulfur isotope variations in the mantle from ion microprobe analyses of micro-sulphide inclusions. *Earth and Planetary Science Letters*, 144-156. https://doi.org/10.1016/0012-821X(89)90042-3

[57] Meinert, L.D. (1992). Skarns and skarn deposits. *Geoscience Canada*, *19*, 145-162.

[58] Meinert, L.D., Dipple, G.M., & Nicolescu, S. (2005). World skarn deposits. *Economic Geology: 100th Anniversary Volume*, 299-336. https://doi.org/10.5382/AV100.11

[59] Ohmoto, H., & Rye, R.O. (1979). Isotopes of sulfur and carbon. *Geochemistry of Hydrothermal Ore Deposits*, 509-567.

[60] Eldridge, C.S., Compston, W., Williams, I.S., Both, R.A., Walshe, J.L., & Ohmoto, H. (1988). Sulfur isotope variability in sediment-hosted massive sulfide deposits as determined using the ion-microprobe, SHRIMP: I. An example from the Rammelsberg orebody. *Economic Geology*, *83*, 443-449. https://doi.org/10.2113/gsecongeo.84.2.453

[61] Kerridge, J.F., Chang, S., & Shipp, R. (1988). Deuterium exchange during acid-demineralization. *Geochimica et Cosmochimica Acta*, *52*, 2251-2255. https://doi.org/10.1016/0016-7037(88)90127-5

[62] Naylor, H., Turrier, P., Vaughan, D.J., Boyce, A.J., & Fallick, A.E. (1989). Genetic studies of redbed mineralization in the Triassic of the Cheshire basin, northwest England. *Journal of the Geological Society*, *146*, 685-699. https://doi.org/10.1144/gsjgs.146.4.0685

[63] Thorpe, R.I. (1999). The Pb isotope linear array for volcanogenic massive sulphide deposits of the Abitibi and Wawa subprovinces, Canada Shield. *The Giant Kid Creek Volcanogenic Massive Sulphide Deposit, Western Abitibi Subprovince, Canada: Economic Geology Monograph*, *10*, 555-576. https://doi.org/10.5382/Mono.10.25

[64] Zartman, R.E., & Doe, B.R. (1981). Plumbotectonics – The model. *Tectonophysics*, *75*, 135-162. https://doi.org/10.1016/0040-1951(81)90213-4

[65] Allegre, C.J., Lewin, E., & Dupre, B. (1988). A coherent crust-mantle model for the uranium-thorium-lead isotopic system. *Chemical Geology*, *70*, 211-234. https://doi.org/10.1016/0009-2541(88)90094-0

[66] Snee, L.W. (2002). Argon thermochronology of mineral deposits: A review of analytical methods, formulations, and selected applications. *U.S. Geological Survey Bulletin*, *2194*, 1-39. https://doi.org/10.3133/b2194

[67] Simmons, S.F., White, N.C., & John, D.A. (2005). Geological characteristics of epithermal precious and base metal deposits. *Economic Geology*, *100*, 485-522. https://doi.org/10.5382/AV100.16

[68] Large, R.R., Bull, S.W., Cooke, D.R., & McGoldrick, P.J. (1998). A genetic model for the HYC deposit, Australia, based on regional sedimentology, geochemistry and sulfide-sediment relationship. *Economic Geology*, *93*, 1345-1368. https://doi.org/10.2113/gsecongeo.93.8.1345

Ар-Ар датування та джерела рудоутворюючих матеріалів свинцево-цинкового родовища На Боп-Пу Сап у районі Чо Дон, Північно-Східний В'єтнам

К.Т. Хунг, П.Т. Х'єу, Н.С. Дак, Н.Д. Хунг

Мета дослідження полягає у вивченні характеристик рудоутворення, моделей генезису та оцінці мінерального потенціалу свинцево-цинкового родовища На Боп-Пу Сап, яке представляє новий тип родовищ у межах Північно-Східного В'єтнаму.

Методика. У роботі використано кілька аналітичних методів, зокрема мікроскопічний аналіз рудних мінералів, ізотопний аналіз сірки та свинцю у рудних сульфідах, Ар-Ар датування серицитових зразків, які сформувалися одночасно з рудними сульфідами, а також вивчення включень у мінералах для визначення температур рудоутворення.

Результати. Польові спостереження свідчать, що рудні поклади проявляються у вигляді свинцево-цинкових жил, пов'язаних із розломами, а також у стратифікованих рудах, що залягають в осадових карбонатних породах раннього девону. Мікроскопічний аналіз показав наявність таких рудних мінералів як галеніт, сфалерит, піротин, пірит і арсенопірит, а також жильних мінералів – кварцу, кальциту й доломіту. Ізотопні значення сірки (δ^{34}S) у галеніті, сфалериті та піриті варіюються від +0.10 до +8.49‰ (середнє значення +4.48‰), що вказує на магматичне походження глибинного джерела. Ізотопні співвідношення свинцю в галеніті (^{206}Pb/^{204}Pb: 18.451-18.651, ^{207}Pb/^{204}Pb: 15.685-15.836, ^{208}Pb/^{204}Pb: 38.909-39.501) вказують на верхньокорове джерело. Ар-Ар датування сериcitу вказало на плато-вік 237.1 ± 2.3 млн років і 242.6 ± 2.4 млн років, яке відповідає часу свинцево-цинкового рудоутворення, що підтверджується синтектонічною текстурою сериciту та рудних сульфідів. Дослідження включень у кальциті, взятому із жил, що містять галеніт, свідчать про помірні температури (201-245°С) і солоності (4.65-8.00 мас.% NaCl еквів.), що вказує на еволюцію систем H₂O – NaCl за різних фізико-хімічних умов. Отримані дані дозволяють класифікувати родовище На Боп-Пу Сап як епітермальне.

Наукова новизна. Свинцево-цинкове родовище На Боп-Пу Сап у північній частині провінції Бак Кан, В'єтнам, є одним із найбільших у районі Чо Дон, що вирізняється значними запасами та унікальним поєднанням металів. Вперше проведено комплексне дослідження часу і походження рудоутворюючих флюїдів цього родовища, включаючи Ар-Ар датування, ізотопний аналіз сірки та свинцю, що дозволило уточнити механізми і джерела рудогенезу, які до цього були недостатньо вивчені.

Практична значимість. Дослідження надає нові знання про генезис і просторово-часову еволюцію свинцево-цинкового рудоутворення в родовищі На Боп-Пу Сап у районі Чо Дон.

Ключові слова: родовище На Боп-Пу Сап, район Чо Дон, свинцево-цинкове рудоутворення, свинець, сірка, Ар-Ар ізотопні дані

Publisher's note